รายงานวิจัยฉบับสมบูรณ์

โครงสร้างเฟส โครงสร้างจุลภาค และสมบัติไดอิเล็กทริกของเซรามิก $Bi_{0.5}(Na_{0.74}K_{0.16}Li_{0.10})_{0.5}TiO_3$-$Ba(Zr_{0.5}Ti_{0.95})O_3$ ที่เตรียมด้วยเทคนิคการเผาไหม้

Phase Formation, Microstructure and Dielectric Properties of $Bi_{0.5}(Na_{0.74}K_{0.16}Li_{0.10})_{0.5}TiO_3$-$Ba(Zr_{0.5}Ti_{0.95})O_3$ Ceramics Prepared via the Combustion Technique

ผู้ช่วยศาสตราจารย์ ดร.ธีระชัย บงการณ์ และคณะ

กรกฎาคม 2558

สัญญาเลขที่ R2558B003

รายงานวิจัยฉบับสมบูรณ์

โครงสร้างเฟส โครงสร้างจุลภาค และสมบัติไดอิเล็กทริกของเซรามิก $Bi_{0.5}(Na_{0.74}K_{0.16}Li_{0.10})_{0.5}TiO_3$-$Ba(Zr_{0.5}Ti_{0.95})O_3$ ที่เตรียมด้วยเทคนิคการเผาไหม้

Phase Formation, Microstructure and Dielectric Properties of $Bi_{0.5}(Na_{0.74}K_{0.16}Li_{0.10})_{0.5}TiO_3$-$Ba(Zr_{0.5}Ti_{0.95})O_3$ Ceramics Prepared via the Combustion Technique

ผศ. ดร. ธีระชัย บงการณ์
ภาควิชาฟิสิกส์ คณะวิทยาศาสตร์ มหาวิทยาลัยนเรศวร

งานวิจัยนี้ได้รับการสนับสนุนงบประมาณจาก
งบประมาณแผ่นดิน มหาวิทยาลัยนเรศวร ประจำปีงบประมาณ 2558

กิตติกรรมประกาศ

งานวิจัยนี้ได้รับกาสนับสนุนงบประมาณจาก งบประมาณแผ่นดิน มหาวิทยาลัยนเรศวร ประจำปีงบประมาณ 2558 ผู้วิจัยขอขอบพระคุณ ณ โอกาสนี้

ขอขอบคุณเจ้าหน้าที่ภาควิชาฟิสิกส์ คณะวิทยาศาสตร์ มหาวิทยาลัยนเรศวร ทุกท่านซึ่งอำนวยความสะดวกเกี่ยวกับอุปกรณ์เครื่องมือต่างๆ

ขอขอบคุณ Science Lab Center คณะวิทยาศาสตร์ มหาวิทยาลัยนเรศวร ที่สนับสนุนเครื่องมือและอุปกรณ์ในการทำวิจัย

ผศ.ดร.ธีระชัย บงการณ์ และคณะ

Research Topic: Phase formation, microstructure and dielectric properties of $Bi_{0.5}(Na_{0.74}K_{0.16}Li_{0.10})_{0.5}TiO_3$-$Ba(Zr_{0.5}Ti_{0.95})O_3$ ceramics prepared via the combustion technique

Researcher: Assist. Prof. Dr.Theerachai Bongkarn

ABSTRACT

The binary lead-free electroceramics with the composition of (1-x)$Bi_{0.5}(Na_{0.74}K_{0.16}Li_{0.10})_{0.5}TiO_3$–$x(BaZr_{0.05}Ti_{0.95})O_3$ or BNKLT-100xBZT with $0.025 \leq x \leq 0.150$ were synthesized via the combustion technique. The results showed how BZT content affects typical properties of a BNKLT-100xBZT system such as phase formation and dielectric properties. The XRD investigation revealed that BNKLT-100xBZT exhibits the coexistence of rhombohedral and tetragonal phases. By BZT addition, the rhombohedral and tetragonal were decreased and increased, respectively. From a dielectric properties investigation, BNKLT-100xBZT showed two dielectric loss peaks at ~ 190 °C and ~ 320 °C and defined as T_d and T_m, respectively. Increasing BZT fraction caused T_m to shift to a lower temperature while insignificantly shifting T_d. The maximum ε_r and ε_{max} with the values of 1,380 and 4,050 were observed from the sample with composition of BNKLT-5BZT. This can be attributed to this composition being located near the MPB region.

CHARPTER I

INTRODUCTION

Rational for the study

Ferroelectric materials have been applied to many electronic and optical devices due to their excellent dielectric, piezoelectric and optical properties. $BaTiO_3$ (BT) has been the most widely studied for lead-free ferroelectric material. This material has shown typical interesting properties such as a large electromechanical coupling factor, high permittivity with an abrupt change near the Curie temperature and a low loss tangent [1]. Many efforts have been made to modify the dielectric properties of $BaTiO_3$ ceramics for typical applications. Substitution of isovalent ions for the host lattice cations in perovskite lattice plays a significant role in these modifications. Substitution of Zr^{4+}, Sn^{4+} for Ti^{4+} results in the formation of $BaZrO_3$ and $BaSnO_3$. These materials form solid solutions with $BaTiO_3$ and alter its structural features, resulting in a shift in phase transition temperature along with modified dielectric properties [2, 3, 4].

Bismuth sodium titanate ($Bi_{0.5}Na_{0.5}TiO_3$, BNT) is a promising perovskite structure lead-free ferroelectric material. This compound has a large remanant polarization (P_r) of 38 $\mu C/cm^2$ with a coercive field (E_c) of 73 kV/cm at room temperature [5]. However, the dielectric properties and the piezoelectric properties of BNT ceramics are significantly lower than the lead-based ceramics [5]. To further improve its properties, a modified BNT composition with some cation dopants has been selected as a substitute for A- site of the perovskite lattice. Lu, et al. [6] investigated on Li and K substituted at the A-site of the BNT lattice. For $Bi_{0.5}(Na_{0.74}K_{0.16}Li_{0.10})_{0.5}TiO_3$ (BNKL1610), the piezoelectric constant d_{33} and electromechanical coupling coefficient K_p are 160 pC/N and 0.35, respectively, which are a great improvement compared with pure BNT ceramics.

Some cation substituted at the A-site lattice, binary system of BNT-based such as BNT-BT [7], BNT-KNN [8] and BNT-BZT [9, 10] is effective technique in improving unsatisfactory properties of BNT ceramics. For example, Parija, et al. [11]

CHARPTER II

RELATED THEORICAL

Piezoelectricity

The word "piezoelectricity" is translated from the Greek word *piezein* which means pressure electricity. This word was discovered by Jacques Curie and Pierre Curie in 1880 [17]. Piezoelectricity is an electromechanical coupling phenomenon occurring in non-centrosymmetric crystalline materials. A piezoelectric crystal will develop an electrical charge in response to an applied mechanical stress to materials (direct effect). Conversely electrical energy can be converted into mechanical energy through the reorientation of dipoles, which rearranges the crystal lattice (converse effect). The piezoelectric effect is linear (first order), producing a strain proportional to the electric field with the displacement directionally dependent on the sign of the applied electric field. The schematic diagram of direct effect and converse effect is illustrated in Figure 1.

Electrostriction is a quadratic (second order) effect in which strain is independent of direction and proportional to the square of the electric field. This phenomenon is the electromechanical response observed in a centrosymmetric crystal, for which no polar properties exist. The elctrostrictive effect is usually very weak with strain on the order of 10^{-11} in simple oxides and 10^{-6} in perovskite oxide. However, some perovskites with high dielectric constants (indicating a high degree of polarizability) can exhibit large electrostrictive electromechanical coupling, with strains on the order of 10^{-3}. High-strain electrostrictors are the preferred materials for high precision controller actuator applications, for they have negligible hysteresis (i.e. no shift of the initial zero position) and do not require electric polling to preferentially orient dipoles or domains [18].

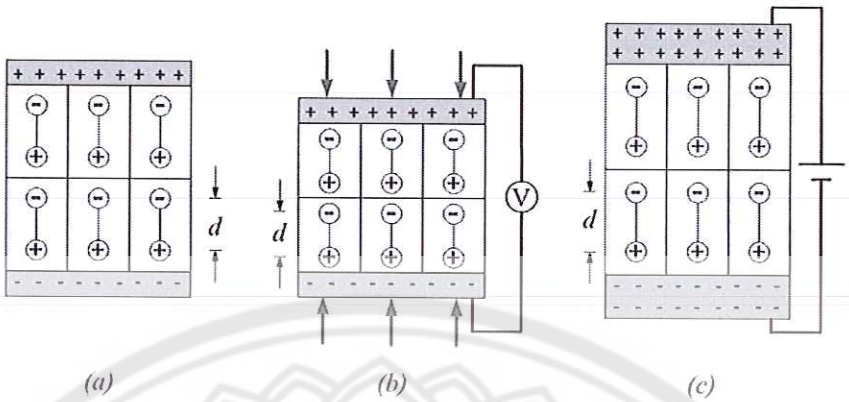

Figure 1 (a) Schematic illustration of electric dipoles within piezoelectric materials, (b) Compressive stresses on materials cause a voltage difference (direct effect), (c) Applied voltage causes materials deform thecrystal lattice (converse effect) [18]

Ferroelectricity

Ferroelectricity (FE) was first discovered in Rochelle salt in 1921. At that time, it was called Seignette-electricity, honoring its discoverer. For the past few decades, ferroelectric materials have received great interest because of their various uses for many applications such as high-permittivity capacitors, pyroelectric sensors, piezoelectric transducers, eletrooptic devices and PTC thermistors [19].

A crystal is ferroelectric when it possesses at least two equilibrium orientations of the spontaneous polarization in the absence of an external electric field. Its spontaneous polarization can be switched between those orientations by an applied electric field. The polar character of the orientation states should represent an absolutely stable configuration in a null field [19]. Among the 32 crystal classes, eleven of them are characterized by the existence of a center of symmetry. The remaining 21 crystal classes do not have a center of symmetry. Thus, it is possible for the 21 groups to (i) have one or more polar axes, and (ii) possess odd-rank tensor properties. The only exception is the group 432. Although it lacks a center of symmetry, it has other symmetry operations that destroy polarity. All non-centrosymmetric point groups exhibit a piezoelectric effect that is defined by a change of electric polarity under applied stress. Out of the twenty piezoelectric classes, ten

possess a unique polar axis. The spontaneous polarization depends on temperature. This is called the pyroelectric effect. Ferroelectric crystals belong to the pyroelectric family, which in addition has a spontaneous polarization which can be reversed by an external electric field. Among all ferroelectric materials, the most extensively studied and widely used are the perovskite crystal. A perfect perovskite structure has a general formula of ABO_3, where A represents a divalent or trivalent cation, and B is typically a tetravalent or trivalent cation. The interrelationship of piezoelectric and subgroup on the basis of symmetry is showed in Figure 2.

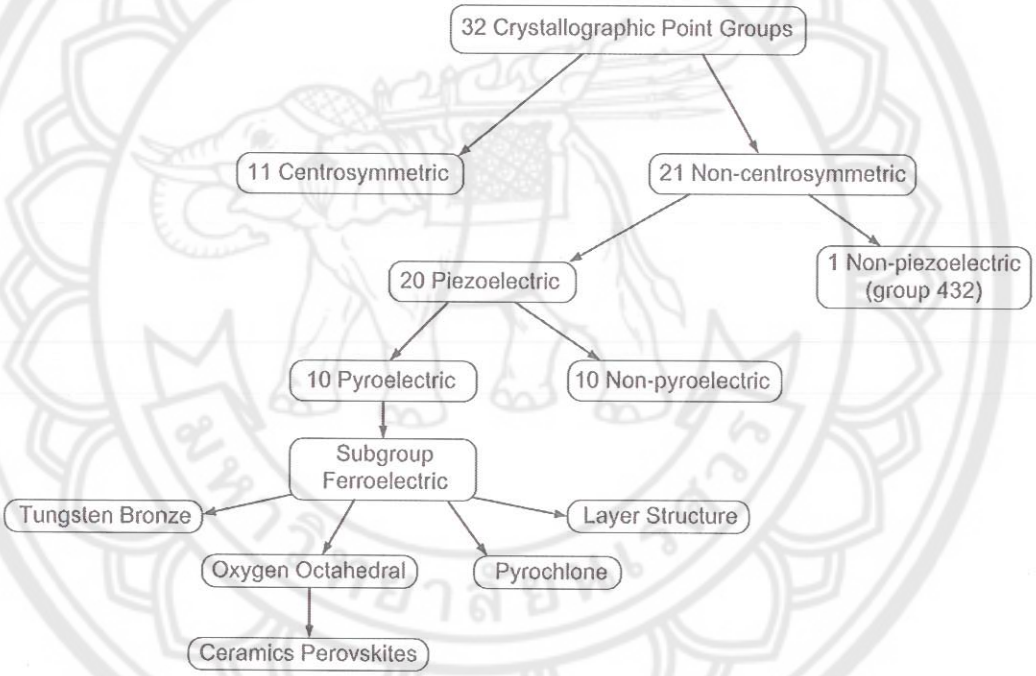

Figure 2 Interrelationship of piezoelectric and subgroup on the basis of symmetry

The origin of ferroelectricity in this family of materials can be explained by the well-known example of barium titanate ($BaTiO_3$). As shown in Figure 3, the Ba^{2+} and Ti^{4+} cations are located at A-site and B-site of the unit cell, respectively [17].

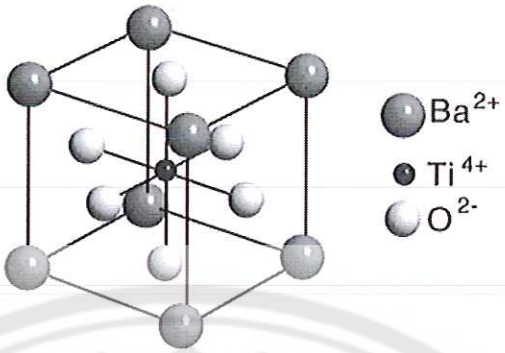

Figure 3 Ion positions in $BaTiO_3$

Typical interested properties of ferroelectric ceramics materials

1. Dielectric properties

Consider two metal parallel plates of area A separated by a distance d in vacuum (Figure 4(a)). Attaching these plates to a simple electric circuit and closing the circuit will result in a transient surge of current that rapidly decays to zero. As shown in Figure 4(b). Given that

$$Q = \int I \, dt \qquad \text{[Eq.1]}$$

The area under the I versus t curve is the total charge that has passed through the circuit and is now stored on the parallel plates.

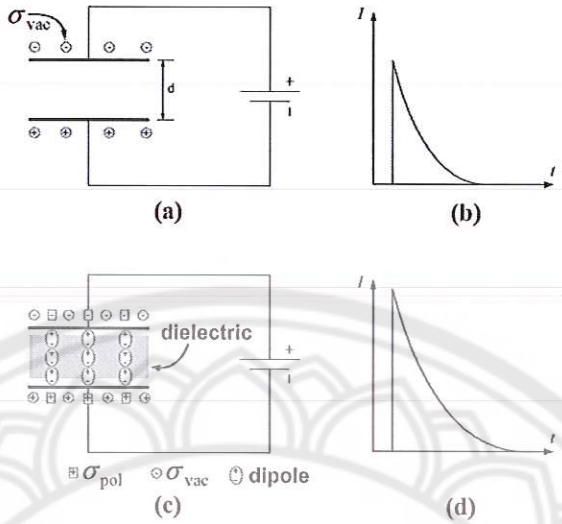

Figure 4 (a) Parallel-plate capacitor of area A and separation d in vacuum attached to a voltage source, (b) Closing of the circuit causes a transient surge of current to flow through the circuit, (c) Parallel-plate capacitor of area A and separation dielectric materials is placed between the plates, (d) Closing of the circuit results in a charge stored on the parallel plates of (c) circuit

Repeating the experiment at different voltages V and plotting Q versus V should yield a straight line (as shown in Figure 5). The well known relationship is

$$Q = CV \qquad \text{[Eq.2]}$$

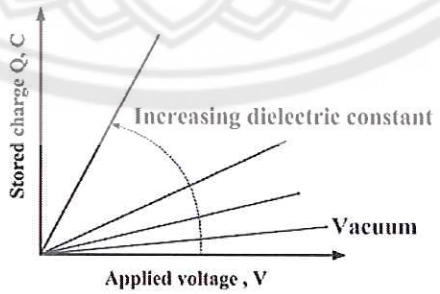

Figure 5 Functional dependence of Q on applied voltage. Slope of curve is related to the dielectric constant of the material

The slope of the Q versus V curve is the capacitance C_{vac} of the parallel plates in vacuum, given by

$$C_{\text{vac}} = \frac{\varepsilon_0 A}{d} \qquad \text{[Eq.3]}$$

Where ε_0 is the permittivity of free space, which is a constant equal to $8.85\times10^{-12}\,\text{C}^2/(\text{J}\cdot\text{m})$.

If a dielectric which can be a gas, liquid or solid is introduced between the plates of the capacitor (Figure 4(c)), the current that flows through the external circuit and is stored on the capacitor plates will increase (Figure 4(d)). Repeating the experiment at different voltages and plotting the total charge stored on the capacitor versus the voltage applied will again result in a straight line but with a larger slope than that for vacuum (Figure 5). The capacitance of the parallel plates is modified to form

$$C = \frac{\varepsilon A}{d} \qquad \text{[Eq.4]}$$

Where ε is the dielectric constant of the material between the parallel plates. The relative permittivity or dielectric constant of a material ε_r is defined as

$$\varepsilon_r = \frac{\varepsilon}{\varepsilon_0} \qquad \text{[Eq.5]}$$

Which when combined with Eq.4 and Eq.5 gives

$$C = \frac{\varepsilon_r \varepsilon_0 A}{d} = \varepsilon_r C_{\text{vac}} \qquad \text{[Eq.6]}$$

Thus ε_r is a dimensionless parameter that compares the charge-storing capacity of a material to that of vacuum.

2. Polarization

By combining of the Eq.2 and Eq.3, the σ_{vac} is the surface charge in vacuum and defined as

$$\sigma_{\text{vac}} = \left[\frac{Q}{A}\right]_{\text{vac}} = \frac{\varepsilon_0 V}{d} = \varepsilon_0 E \qquad \text{[Eq.7]}$$

When a dielectric is introduced between the parallel plates (Figure 4(c)), the surface charge on the parallel plates increases to

$$\left[\frac{Q}{A}\right]_{die} = \frac{\varepsilon_0 \varepsilon_r V}{d} = \sigma_{vac} + \sigma_{pol} \qquad \text{[Eq.8]}$$

Where σ_{pol} is the excess charge per unit surface area present on the dielectric surface. The σ_{pol} is numerically equal to the polarization (P) of the dielectric.

$$P = \sigma_{pol} \qquad \text{[Eq.9]}$$

The surface charge on the parallel plates is defined as dielectric displacement (D) which when combined with Eq.7 and Eq. 9 gives

$$D = \sigma_{vac} + \sigma_{pol} = \varepsilon_0 E + P = \varepsilon \varepsilon_0 E \qquad \text{[Eq.10]}$$

Further combining Eq.7 to Eq.10, one sees that

$$P = (\varepsilon_r - 1)\varepsilon_0 E = \chi_{die} \varepsilon_0 E \qquad \text{[Eq.11]}$$

Where $\chi_{die} = \frac{\sigma_{pol}}{\sigma_{vac}}$ and defines the dielectric susceptibility of the material.

3. Hysteresis loop

Ferroelectric materials can switch their spontaneous polarization by an applied electric field. The reversal polarization can be observed by measuring the ferroelectric hysteresis as shown in Figure 6. As an applied electric field is increased, the polarization increases rapidly and reaches a saturation polarization (P_s). Upon decreasing an electric field back to zero, polarization does not fall to zero. Some of the domains in crystal remain aligned in the positive direction; hence the crystal will show a remanent polarization (P_r). Upon reversing the direction of electric field, the polarization is removed and a net zero polarization is occurs at a coercive field (E_c). Further increases in the reverse field lead to saturation of polarization in the opposite direction.

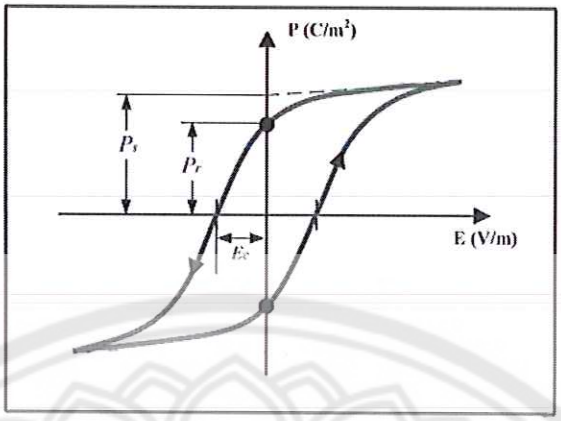

Figure 6 A typical ferroelectric hysteresis loops

4. Phase transition and Curie temperature

All ferroelectric materials have a transition temperature called the Curie temperature (T_c) [20]. At a temperature $T > T_c$ the crystal does not exhibit ferroelectricity. While $T < T_c$, the crystal shows ferroelectric characteristics. On decreasing the temperature through the Curie point, a ferroelectric crystal undergoes a phase transition from a non-ferroelectric phase to a ferroelectric phase. If there are more than one ferroelectric phases, the temperature at which the crystal transforms from one ferroelectric phase to another is called the transition temperature.

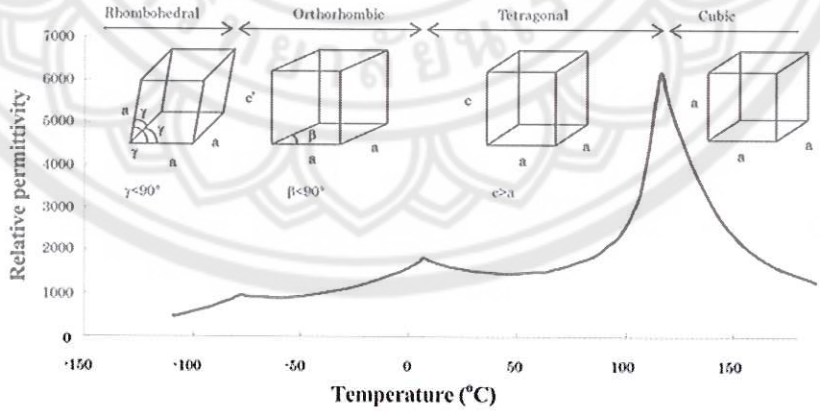

Figure 7 Variation of relative permittivity with temperature for $BaTiO_3$ [17]

Figure 7 shows the variation of the relative permittivity with temperature of $BaTiO_3$. The crystal is cooled from its paraelectric cubic phase to the ferroelectric

tetragonal, orthorhombic, and rhombohedral phases, respectively. Near the Curie temperature or phase transition temperatures, thermodynamic properties including dielectric, elastic, optical, and thermal constants show an anomalous behavior. This is due to a distortion in the crystal as the phase structure changes. The temperature dependence of the dielectric constant above the Curie point ($T > T_c$) in ferroelectric crystals is performed by the Curie-Weiss law:

$$\varepsilon_r = \frac{A}{T - \theta_c} \qquad \text{[Eq.12]}$$

Where A is a constant for a given material and θ_c is a temperature near to but not identical with the Curie temperature [17].

Typical ferroelectric matrials: Barium titanate (BT)

At high temperature, barium titanate ($BaTiO_3$) is cubic structure with the ion arranged as in Figure 8(a). Below the Curie point (approximately 120°C), the structure is slightly distored to tetragonal with the *c/a* ratio of around 1.01 and is stable. The spontaneous polarization is along one of the (001) directions in the original cubic structure. Between 0°C and -90°C, the ferroelectric orthorhombic phase is stable with the polarization along one of the (110) directions in the original cubic structure. When decreasing the temperature below -90°C the phase transition from the orthorhombic to ferroelectric rhombohedral phase leads to polarization along one of the [111] cubic directions. The phase transition behavior of $BaTiO_3$ is illustrated in Figure 7.

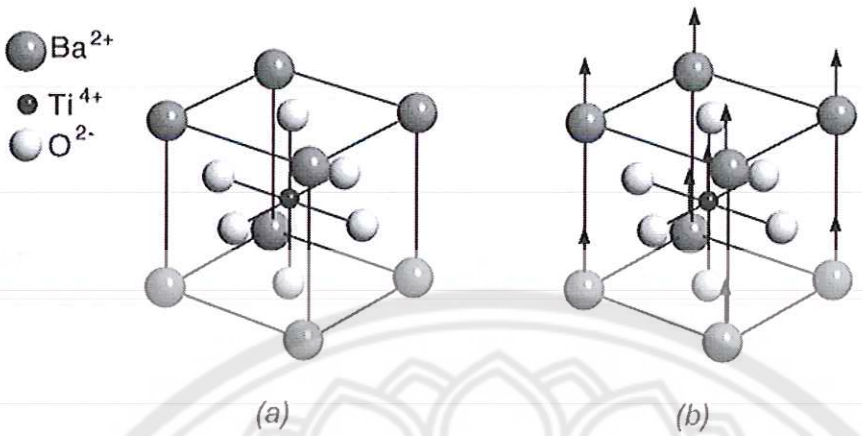

Figure 8 The crystal structures of BaTiO3 (a) Above Curie point show cubic structure, (b) Below Curie point the structure is tetragonal form with Ba^{2+} and Ti^{4+}slightly shifted relative to O^{2-}

The spontaneous polarization on cooling $BaTiO_3$ below the Curie point is due to changes in the crystal structure. As shown in Figure 8(b). Below Curie point, the structure of $BaTiO_3$ changes from a cubic to a tetragonal phase. The center of positive charges (Ba^{2+} and Ti^{4+} ions) is slightly shifted relative to negative charges (O^{2-} ion) which leads to the formation of electric dipoles. The spontaneous polarization developed is the net dipole moment produced per unit volume for the dipoles pointing in a given direction.

Typical preparation technique for ferroelectric ceramics

Solid state reaction method

The first step in the conventional method for preparing ferroelectric ceramics based on the solid state reaction method is weighing the starting materials according to the stoichiometric composition. After mixing and grinding, the mixture is usually calcined to produce the desired compound by combination reaction. Synthesis reaction of a compound is caused from the chemical reaction of raw materials, which occurs by atomic diffusion among particles at temperatures below the melting point of these raw materials. Using the diffusion laws, an equation describing the speed of solid phase reaction can be derived;

$$\left(1-(1-x)^{1/3}\right)^2 = \frac{2D't}{r^2} = 2Dt \qquad \text{[Eq.13]}$$

with

$$D = C\exp\left(\frac{-Q}{RT}\right) \qquad \text{[Eq.14]}$$

Where C is a constant related to the radius r of the particle, R is the gas constant, T is the absolute temperature and Q is the activation energy. This equation shows that the volume ratio x of the product increases with the increase of reaction temperatures T and reaction time t.

After calcination, the calcined powders are pressed in the mold and sintered at a higher temperature than that of the calcination. The ceramic products are densified after sintering and the grain size of the ceramic increases with increased sintering temperature.

Sol-gel method

The sol-gel process uses inorganic or metal-organic as precursors [21]. In aqueous or organic solvents, the precursors are hydrolyzed and condensed to form inorganic polymers composed of M-O-M bonds. In case of inorganic precursors, hydrolysis proceeds by the removal of a proton from an aqua ion to form a hydroxo (-OH) or oxo (=O) ligand. Condensation reactions involving the hydroxo ligands result in the formation of bridging hydroxyl (M-p(OH)-M) or oxo (M-O-M) bonds. Normally, monomeric aqueous ions are only stable at low pH and various monomeric or oligomeric anions are observed at high pH. At intermediate pH, well-defined polynuclear ions are often a stable solution. The the metal solubility is normally limited there. When it is exceeded, it results in the precipitation of oxyhydroxides or oxides.

Co-precipitation method

The concept of the co-precipitation technique is to transfer impurities to a precipitate concurrently with the deposition of some primary substances. Co-precipitation proceeds in two stages. In the first stage, the impurity is trapped either on the surface or inside the growing particles. If the growing particles have a crystal structure, then the impurity will become localized at regions of the solid phase with a perfect structure. During rapid precipitation, the growing particles will trap non-

equilibrium impurities, which are usually inhomogeneously distributed through the volume of the solid phase. In the second stage, the concentration of defects within the precipitate decreases and the particles are flocculated. Impurities trapped during the first stage return either partially or completely to the medium. The concentration of impurities in the solid phase becomes equalized. The crystals acquire an equilibrium composition that depends only on the composition and temperature of the medium.

Hydrothermal synthesis method

Hydrothermal synthesis is the crystallizing of substances from high-temperature aqueous solutions at high vapor pressures. Hydrothermal synthesis can be defined as a method of synthesizing single crystals which depends upon the solubility of minerals in hot water under high pressure. The crystal growth is formed in an apparatus consisting of a steel pressure vessel. A gradient of temperature is maintained at the opposite ends of the growth chamber. The hotter end dissolves the nutrient and the cooler end causes seeds to take on additional growth.

Combustion technique

The combustion synthesis method is modified from the solid state reaction method. It is an attractive method for preparing electroceramic materials, which involves a self-sustained reaction between reaction materials and fuel (e.g., urea, glycine, citric acid). The reaction converts the initial mixture typically to a fine well-crystalline powder of desired composition [12-14]. The combustion reaction gives out the energy that can be effectively applied to the raw materials. The released energy speeds up the chemical reaction of the raw materials and also decreases the reaction temperature. Moreover, the combustion technique is simple, inexpensive and less time consuming in comparison with other methods.

Sintering process

After the powders are synthesized, the pellets should heat at high temperature to produce the desired microstructure. This stage is called in term sintering. The process of sintering consists of three stages: an initial, intermediate, and final stage [29]. For an initial stage, the green body has a low density and lacking in physical integrity. There is a small degree of adhesion between adjacent particles. After heat treatment, the local point of contact initially joins without shrinkage. This is

accompanied by a smoothing of the free surface of the particles. After that, the neck formation at the contact point occurs (Figure 9). If the relative green density after the forming of the particle was 60%, the density after the initial stage would be about 70% of the theoretical density.

In an intermediate state, the significant results are the neck growth, pores forming arrays of interconnected channels and particle centers approaching one another. The high curvatures exhibited in the initial stage are assumed to have been eliminated. Densification is assumed to occur by the pore simply shrinking to reduce their radius. This stage is considered to have a relative density of 90% of the theoretical density. In the final stage, the pores are pinch off and become isolated at the grain corners. In an idealized model, the pores are assumed to shrink continuously and may disappear altogether.

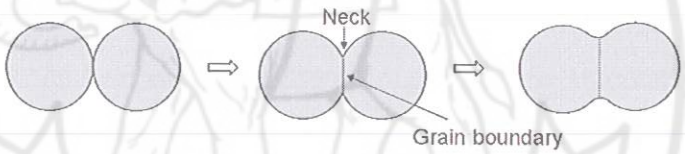

Figure 9 Schematic of two particles partly joined together on sintering process characterization techniques for ferroelectric ceramics [19]

Typical characterizations for ferroelectric ceramics

Thermal analysis (DSC and TGA)

The basis of Differential scanning calorimetry (DSC) is the measurement of heat flow which is plotted against the temperature of the furnace or the time to get a thermogram. The curve obtained in DSC is between dH/dt in $mJ \cdot s^{-1}$ or $mcal \cdot s^{-1}$ as a function of time or temperature. A typical DSC curve is shown in Figure 10. The deviation observed above the base (zero) line is called an exothermic transition and the deviation below is called endothermic transition. The area under the peak is directly proportional to the heat evolved or absorbed by the reaction, and the height of the curve is directly proportional to the rate of reaction

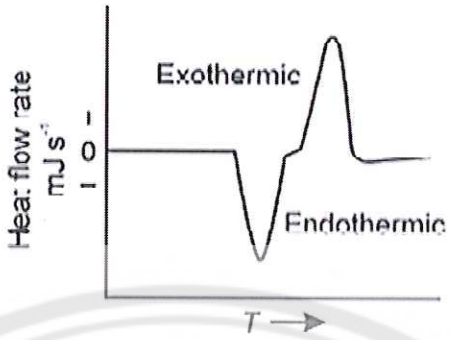

Figure 10 A typical DSC curve [22]

The block diagram of a DSC instrument as shown in Figure 11, essentially works on the temperature control of two similar specimen holder assemblies. The left half of the block diagram represents the circuit for differential temperature control while the right hand side represents average temperature control. In the average temperature control circuit, the temperature of the sample and reference are measured and averaged and the heat output of the average heater is automatically adjusted so that the average temperature of the sample and reference increases at a linear rate. The differential temperature control circuit monitors the difference in temperature between the sample and reference and automatically adjusts the power to either the reference or sample chambers to keep the temperatures equal. For getting a thermogram, the temperature of the sample is put on the *x*-axis and the difference in power supplied to the two differential heaters is displayed on the *y*-axis.

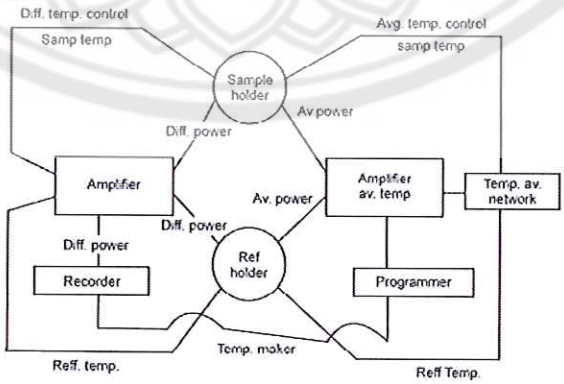

Figure 11 Block diagram of a DSC instrument [22]

Thermogravimetric analysis (TGA) is an analytical technique used to determine a material's thermal stability and its fraction of volatile components by monitoring the weight change that occurs as a specimen is heated. The measurement is normally carried out in air or in an inert atmosphere, such as Helium or Argon, and the weight is recorded as a function of increasing temperature. Sometimes, the measurement is performed in a lean oxygen atmosphere (1 to 5% O_2 in N_2 or He) to slow down oxidation. In addition to weight changes, some instruments also record the temperature difference between the specimen and one or more reference pans (differential thermal analysis, or DTA) or the heat flow into the specimen pan compared to that of the reference pan (differential scanning calorimetry, or DSC). The latter can be used to monitor the energy released or absorbed via chemical reactions during the heating process.

X-ray diffraction (XRD)

In X-ray diffraction, a collimated of mono-chromatic X rays between 0.5 – 2Å wavelength which strike a sample and are diffracted by the crystal planes present Bragg's law.

$$\lambda = 2d\sin\theta \qquad \text{[Eq.15]}$$

Bragg's law relates to the spacing between planes, d, to the diffraction angle, 2θ, which is scanned to pick up diffraction from the different crystal planes present. The azimuthal orientation of the diffraction beams also reveals the crystalline orientation. Distortions or broadening of the diffraction beams carry information on crystal strain and grain size. The schematic illustration of XRD analysis is illustrated in Figure 12.

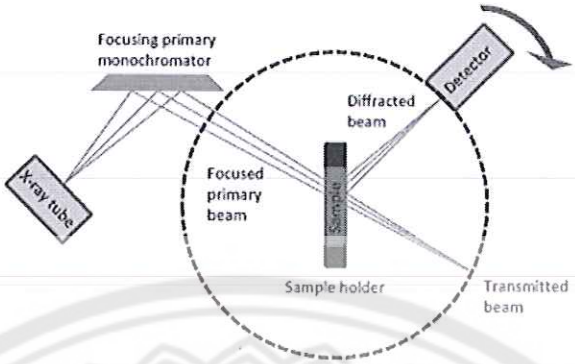

Figure 12 Schematic illustration of the diffractometer method of crystal analysis

Scanning electron microscope (SEM)

Scanning electron microscopy (SEM) is one of the most versatile and well known analytical techniques. Compared to a conventional optical microscope, an electron microscope offers advantages including high magnification, large depth of focus, great resolution and ease of sample preparation and observation. Electrons generated from an electron gun enter a surface of a sample and generate many low energy secondary electrons. The intensity of these secondary electrons is governed by the surface topography of the sample. An image of the sample surface is therefore constructed by measuring secondary electron intensity as a function of the position of the scanning primary electron beam. In addition to secondary electron imaging, backscattered electron imaging and Energy Dispersive X-ray (EDX) Analysis are also useful tools widely used for chemical analysis. The intensity of backscattered electrons generated by electron bombardment can be correlated to the atomic number of the element within the sampling volume. Hence, qualitative elemental information can be revealed. The characteristic X-rays emitted from the sample serve as fingerprints and give elemental information of the samples including semi-quantitative analysis, quantitative analysis, line profiling and spatial distribution of elements. A schematic diagram of the basic design of a SEM instrument is shown in Figure 13.

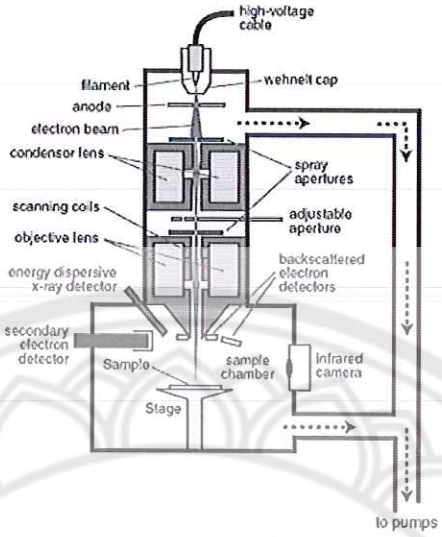

Figure 13 Schematic diagram of the basic design of a SEM [22]

Transmission electron microscope (TEM)

Figure 14 shows a schematic outline of a TEM. A TEM contains four parts: electron source, electromagnetic lens system, sample holder, and imaging system.

TEM works like a slide projector. A projector shines a beam of light which transmits through the slide. The patterns painted on the slide only allow certain parts of the light beam to pass through. Thus the transmitted beam replicates the patterns on the slide, forming an enlarged image of the slide when falling on the screen.

TEM works the same way except that they shine a beam of electrons (like the light in a slide projector) through the specimen (like a slide). However, in TEM, the transmission of the electron beam is highly dependent on the properties of the material being examined. Such properties include density, composition, etc. For example, porous material will allow more electrons to pass through while dense material will allow less. As a result, a specimen with a non-uniform density can be examined by this technique.

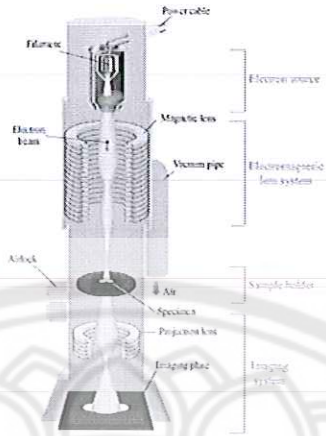

Figure 14 The schematic outline of a TEM [22]

Dielectric measurement

Parallel plate capacitor system uses a parallel plate capacitor as a sample holder, with the material under the test sandwiched between. This method requires an impedance analyzer or LCR meter. The measurements are at low frequencies, typically below 1 GHz. The material is stimulated by an AC source and the actual voltage across the material is monitored. The material test parameters are derived by knowing the dimensions of the material and by measuring its capacitance and dissipation factor. After putting a sample into a sample holder, a capacitor is formed. The parallel plate method involves sandwiching a thin sheet of material between two electrodes to form a capacitor. The measured capacitance is then used to calculate permittivity. The schematic diagram for this technique is shown in Figure 15.

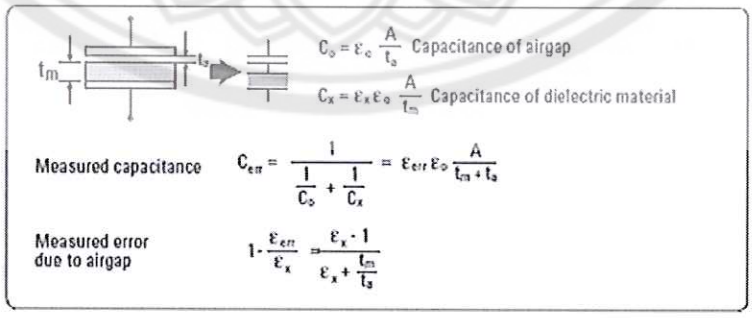

Figure 15 Diagram for dielectric measurement (parallel plate method) [22]

Ferroelectric measurement

A *P-E* loop for a device is a plot of the charge or polarization developed, against the electric field applied to that device (*E*) at a given frequency.

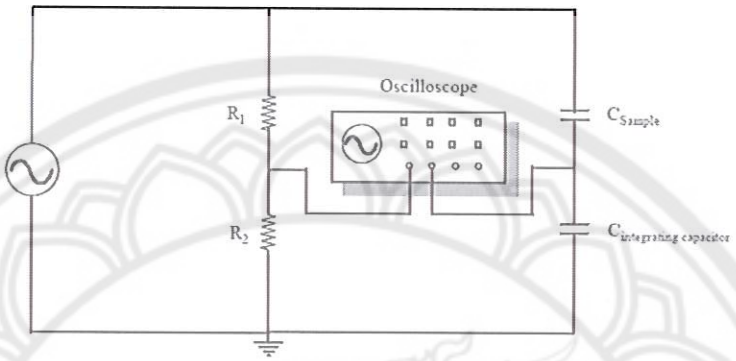

Figure 16 Schematic of a circuit for *P-E* measurement [22]

A schematic of the experimental setup is shown in Figure 16. Here the field applied across the sample is attenuated by a resistive divider, and the current is integrated into charge by virtue of a large capacitor in series with the sample. Both these voltages are then fed into the X and Y axes of an oscilloscope to generate the *P-E* loop. The applied voltage was usually a sinusoid at mains frequency as this was the simplest method to generate the required voltage and current.

CHARPTER III

LITERATURE REVIEWS

This chapter is composed of several reports whose topics relate to this work. The viewpoints of this section include: the effects of zirconium content on structure and typical properties of $Ba(Zr_xTi_{1-x})O_3$ system, various techniques for improving BNT-properties, and the application of the combustion technique for synthesizing ferroelectric ceramics.

Barium zirconium titanate

The substitution of Zr^{4+} to Ti^{4+} to form $Ba(Zr_xTi_{1-x})O_3$ or BZT became interesting for more fundamental studies and also for some novel applications due to its excellent dielectric, tunability and promising piezoelectric and relaxor properties. The ferroelectric properties of BZT are largely dependent on the amount of Zr^{4+} substitution. At room temperature, this ceramics show normal ferroelectric behavior for $0 < x < 0.20$ and relaxor behavior when $x > 0.25$ [23].

As mentioned, $BaTiO_3$ exhibits a cubic phase at high temperature. By decreasing the temperature, the crystal structure is slightly distorted. The first phase transition occurs at ~120 ^{o}C and is called Curie temperature (T_c), in which the structure changes from a cubic to a tetragonal structure [17]. The next phase transition point, defined as T_{o-t} (~ 0 ^{o}C), is the phase transition-temperature from a tetragonal to an orthorhombic structure [17]. At -90 ^{o}C, the crystal structure is transformed from orthorhombic to rhombohedral. This point is defined as T_{r-o} [17]. Substitution of Zr^{4+} to Ti^{4+} induces T_{r-o} and T_{o-t} to increase, whereas T_c decreases [24]. When the Zr content is ~15 at.%, all the above three phase transition temperatures T_{o-t}, T_{r-o} and T_c merge near room temperature as reported by Dixit et al. [23]. The schematic diagrams of phase transition temperatures shifted and pinch phase transition are shown in Figure 17(a) and (b), respectively.

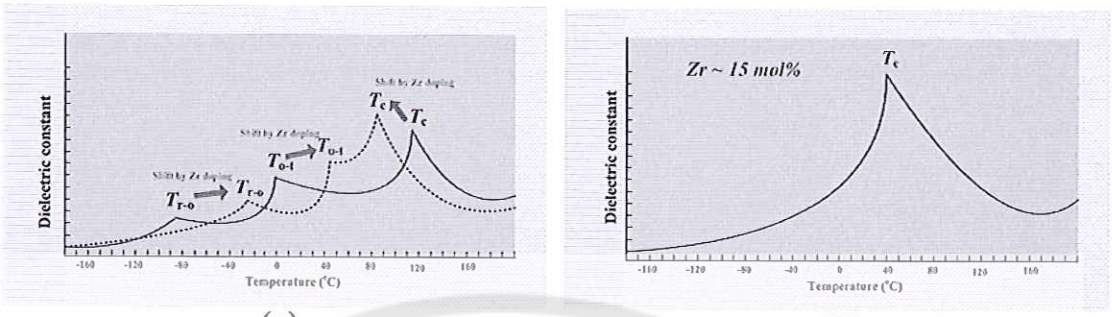

Figure 17 Schematic diagram of how the Zr doped affects the phase transition temperatures of barium titanate

Effects of zirconium content on structure and typical properties of BZT ceramics

1. Crystal structure

There are different reports about how the crystal structure of $BaTiO_3$ is changed due to Zr substitution [24-27]. Some groups reported the crystal structure of $BaTiO_3$ shows a tetragonal phase and substitution of Zr caused the tetragonality to increase. Chen, et al. [26] studied the crystal structure of $Ba(Zr_xTi_{1-x})O_3$ with $0.05 \leq x \leq 0.20$. The result demonstrated that BZT exhibited a tetragonal structure in all compositions. By increasing zirconium substitution, the lattice parameter a was increased while the lattice parameter c decreased. For $Ba(Zr_xTi_{1-x})O_3$ with $x = 0.2$, a c/a ratio of around 1.01 was observed as shown in Figure 18. Huang *et al.* [28] investigated the structure of $Ba(Zr_xTi_{1-x})O_3$ with x lower than 15 mol% by using XRD patterns. The results suggested that by increasing the zirconium content, the lattice parameters a and c were increased and the tetragonality approached 1 at 15 mol% zirconium substitution. Neirman, et al. [29] has also pointed out that as zirconium increased, both lattice parameters c and a were increased because the larger Zr^{4+} ionic radius (0.087 nm) is larger than that of Ti^{4+} (0.068 nm). However, the ratio of c/a decreased and when the zirconium content was higher than 10 mol%, the lattice constant increased in direct proportion to the increasing zirconium content.

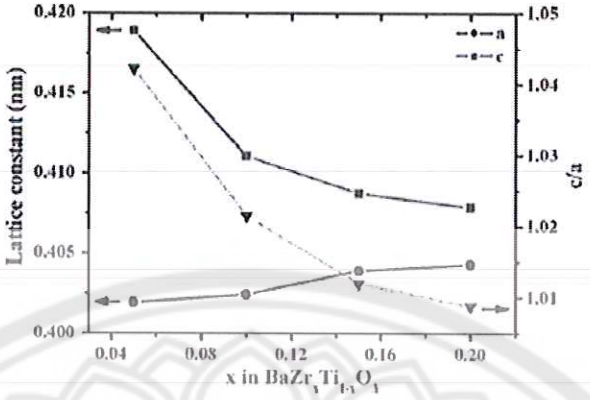

Figure 18 Dependences of the *a*- and *c*-axis lattice constants and *c/a* ratio (right hand side ordinate) on Zr/Ti ratio at room temperature [26]

Many researchers have reported the crystal structure of BZT from other viewpoints. Dixit, et al. [23] investigated the phase transition behavior of $Ba(Zr_xTi_{1-x})O_3$ with $0 \leq x \leq 0.4$. The report explained that the crystal structure of BZT depended upon the amount of Zr. BZT may have a tetragonal, orthorhombic, rhombohedral or cubic structure at room temperature. However, this report did not clearly explain the crystal structure of BZT for each composition. Kuang, et al. [24] studied the influence of Zr doped on properties of $Ba(Zr_xTi_{1-x})O_3$ with $0 \leq x \leq 0.12$. The report suggested that BZT exhibited a tetragonal phase at room temperature and that the crystal structure underwent a transformation from tetragonal to orthorhombic when zirconium content was increased. Binhayeeniyi, et al. [30] studied the crystal structure of $Ba(Zr_xTi_{1-x})O_3$ with $0 \leq x \leq 0.2$ using the Raman spectra and the XRD patterns. The report showed that is not possible to identify the crystalline phase of $Ba(Zr_xTi_{1-x})O_3$ with $0.00 \leq x \leq 0.02$ composition due to the close proximity of the diffraction angles. When the Zr content reached 10 mol%, the analysis results indicated that the crystal structure of BZT transformed from the orthorhombic to the rhombohedral phase and the structure was changed to a cubic phase when the zirconium content reached 20 mol%. The difference in the reports about the crystal structure of BZT*x* were summarized and are shown in Figure 19.

Report	x = 0-5	x = 5-10	x = 10-15	x = 15-20
[5], [6]	Tetragonal			
[8]	Orthorhombic	Tetragonal		
[9]	*	Orthorhombic	Tetragonal	
[33]	Orthorhombic		Rhombohedral	

Note: * = unidentified phase*

Figure 19 Phase identification of BZT ceramics with variation of mol% zirconium of *x* reported by several literatures

2. Dielectric constant

The substitution of Zr^{4+} to Ti^{4+} highly influenced the dielectric constant of $BaTiO_3$ [24, 26, 28, 31]. However, the effects of zirconium content on the dielectric properties of BZT show different characteristics. Chen, et al. [26] investigated the temperature dependence of the dielectric permittivity of BZT ceramics with various stoichiometric percentages of zirconium from 5 to 20 mol% (Figure 20). The results demonstrated that the value of maximum permittivity decreased as the zirconium content increased. Meanwhile, the permittivity of BZT ceramics with a higher zirconium content exhibited broad peaks. The broadness indicated the diffuse phase transition from a ferroelectric to a paraelectric phase. Moreover, the diffuse transition behavior was enhanced with increasing zirconium content, indicating a composition induced diffuse transition. Yu, et al. [31] investigated the dielectric properties of $Ba(Zr_xTi_{1-x})O_3$ with $0 \leq x \leq 0.3$. The study showed permittivity displays an irregular change with variations of Zr concentration, and shows a maximum of 46,000 at a Zr concentration of $x = 0.08$ in region I (Figure 21). This might be partially related to its grain size variation, which depends on both the processing and Zr concentrations. The increase and decrease of the maximum dielectric constant due to an increase of the zirconium content as reported by other groups is exhibited and summarized in Figure 22.

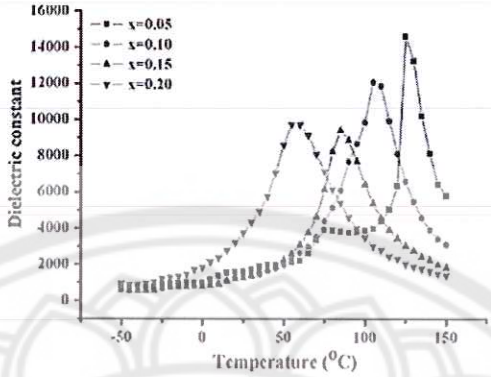

Figure 20 Temperature dependence of the relative permittivity of $Ba(Zr_xTi_{1-x})O_3$ ceramics at 1 kHz [26]

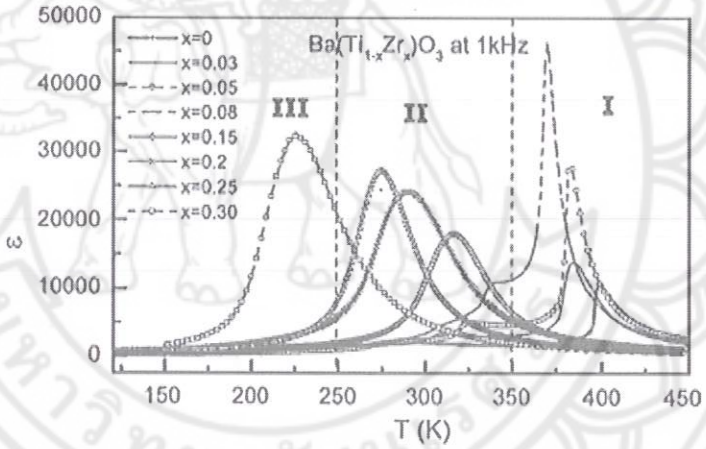

Figure 21 Temperature dependence of dielectric constant ε at 1 kHz for the $Ba(Zr_xTi_{1-x})O_3$ ceramics with x = 0, 0.03, 0.05, 0.08, 0.15, 0.2, 0.25 and 0.3 [31]

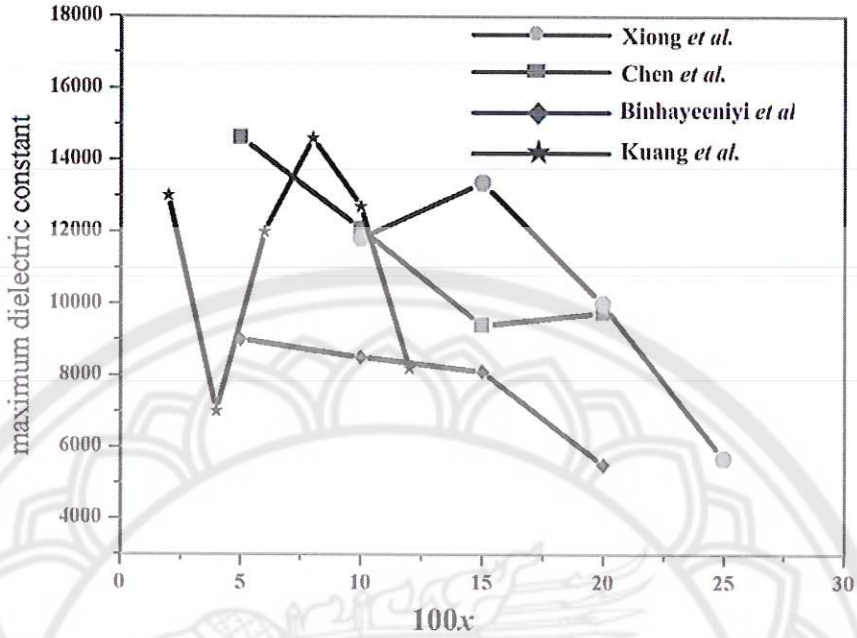

Figure 22 Variation of maximum dielectric constant of $Ba(Zr_xTi_{1-x})O_3$ from the literatures

3. Phase transition temperatures

The transition temperature of $BaTiO_3$ can be shifted when doped with isovalent ions substitution. Ba^{2+} can be replaced by isovalent ions with r_{12} radii between 130 and 160 pm (such as Pb^{2+}, Sr^{2+} and Ca^{2+}). Ti^{4+} can be replaced by isovalent ions with r_6 radii between 60 and 75 pm (such as Zr^{4+} and Sn^{4+}). For Ti^{4+} replaced by Zr^{4+}, they reduce T_c but raise the temperature of the other two transitions [17].

Nanakorn, et al. [21] studied the phase transition temperature of $Ba(Zr_x Ti_{1-x})O_3$ ceramics with $0.00 \leq x \leq 0.08$ from the temperature dependence of the dielectric curve as shown in Figure 23. They found that with increasing Zr content (0–5 mol %), the transition temperatures from tetragonal to orthorhombic structure (T_1) shifts toward higher temperatures. Transition temperatures from orthorhombic to rhombohedral (T_2) are clearly shown only at $x = 0.05$. At $x = 0.08$, the diffuse phase transition occurs resulting in an unclear phase transition temperature (T_1 and T_2). The transition temperatures and Curie temperatures of the BZT based compositions were recorded and are summarized in Table 1.

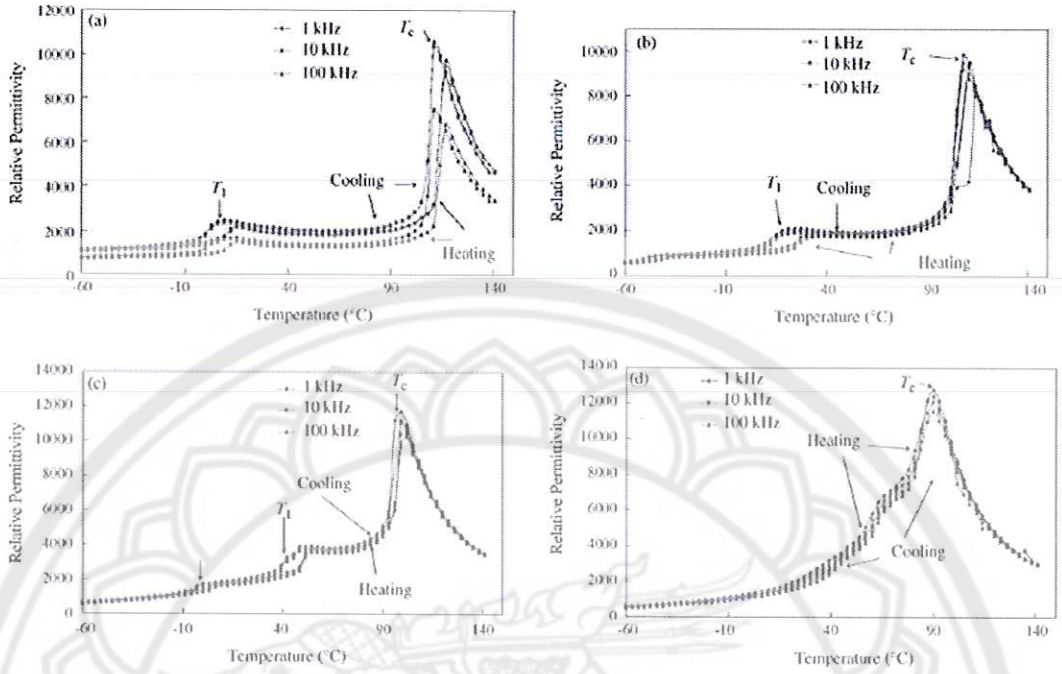

Figure 23 Temperature dependence of the relative permittivity for $Ba(Zr_xTi_{1-x})O_3$ ceramics with (a) $x = 0$ sintered at 1300 °C, (b) $x = 0.02$ sintered at 1350 °C, (c) $x = 0.05$ sintered at 1450 °C and (d) $x = 0.08$ sintered at 1400 °C at 1 kHz, 10 kHz and 100 kHz [21]

Table 1 The phase transition temperature (T_1, T_2 and T_c) of BZT ceramics [21]

$Ba(Zr_xTi_{1-x})O_3$	T_1 (°C)	T_2 (°C)	T_c (°C)
$x = 0.00$	6	-	117
$x = 0.02$	18	-	111
$x = 0.05$	42	0	102
$x = 0.08$	-	-	90

Kuang, et al. [24] plotted T_c (phase transition temperature from tetragonal to cubic structure), T_{o-t} (phase transition temperature from orthorhombic to tetragonal structure) and ε_m (maximum dielectric permittivity) as a function of zirconium content at 10 kHz for $Ba(Zr_xTi_{1-x})O_3$ ceramics with $0 < x < 0.12$ (Figure 24). The T_{o-t}

increased nonlinearly from 33 to 80 °C with increasing x from 0.02 to 0.10, respectively. Furthermore, the T_{o-t} peak decreased with increasing x. The phenomenon of decreasing T_c with increasing x can be explained in two ways. The first is because the radius of the Zr^{4+} is larger than that of the Ti^{4+} ion. The substitution of Zr^{4+} for Ti^{4+} will weaken the bonding force between the B-site ion and the oxygen ion of the ABO_3 perovskite structure. As the B–O bonds are weakened, the B-site ion can resume its position only when the tetragonal ferroelectric is at lower temperature, so the phase transition temperature is reduced. The second reason is because the weakening of the B–O bonds leads to a weaker distortion of the octahedron and the replacement also might induce a break of the cooperative vibration of the B–O chains. When this happens the *c/a* ratio is decreased. This break is responsible for the T_c of the BZT system, and thus a drop in Curie temperature was observed [24]. The values of T_c and T_{o-t} approached the same value when x is raised to ~0.12. The phase transition temperature from rhombehedral to orthorhombic (T_{r-o}), phase transition temperature from orthorhombic to tetragonal (T_{o-t}) and Curie temperature (T_c) dependence with zirconium content observed from literatures are listed in Table 2.

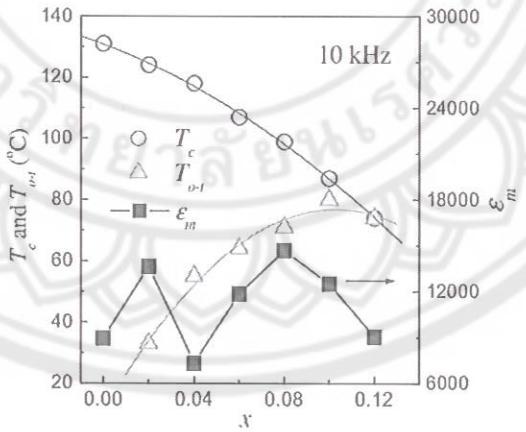

Figure 24 Phase transition temperature T_c, T_{o-t} and maximum dielectric permittivity ε_m as functions of zirconium content x at 10 kHz for $Ba(Zr_xTi_{1-x})O_3$ ceramics [24]

Table 2 $T_{r\text{-}o}$, $T_{o\text{-}t}$ and T_c as a function of zirconium content reported by literatures

Report	Composition of $100x$ of $Ba(Zr_xTi_{1-x})O_3$	$T_{r\text{-}o}$ (^oC)	$T_{o\text{-}t}$ (^oC)	T_c (^oC)
Chen, et al.[26]	5			102
	10			89
	15			74
	20			55
Xiong, et al.[32]	10			90
	15			70
	20			40
	25			0
Kuang, et al.[24]	2		30	125
	4		55	118
	6		65	109
	8		70	100
	10		81	901
	12		75	75
Yu, et al.[31]	3	-33	27	107
	5	-13	47	102
	8	37	57	92
	15	-	-	37
	20	-	-	17
	25	-	-	-3
	30	-	-	-53

4. Ferroelectric polarization

The effects of zirconium content on the ferroelectric properties of BZT were investigated by Chen, et al. [26]. The results of well-behaved hysteresis loops of $Ba(Zr_xTi_{1-x})O_3$ with x = 0.05, 0.10, 0.15 and 0.20 are shown in Figure 25. It was found that the *P-E* hysteresis loop showed slimmer characteristics when the zirconium content increased.

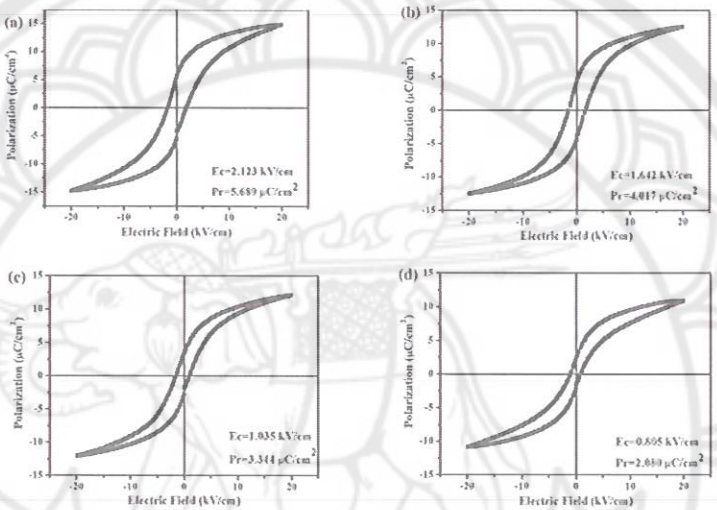

Figure 25 *P-E* Hysteresis loops of $Ba(Zr_xTi_{1-x})O_3$ ceramics at room temperature and 1 kHz with (a) x = 0.05, (b) x = 0.10, (c) x = 0.15, and (d) x = 0.20 [26]

Figure 26 shows the plot of the coercive electric field (E_c) and the remanent polarization (P_r) versus the stoichiometric percentage of zirconium. Both E_c and P_r decreased as zirconium content increased. Variation in remanent polarization in BZT ceramics can be explaine by the difference of radius in Zr^{4+} and Ti^{4+}. The decrease in E_c values with increasing zirconium content could be attributed to the increase in grain size as a result of the same sintering temperature. It is well known that a reversal polarization process in the ferroelectric domain is much easier inside a large grain than in a small grain.

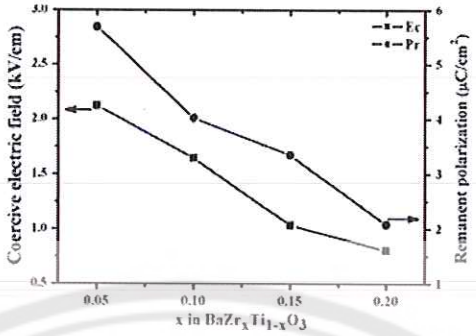

Figure 26 The E_c and P_r dependences of Zr/Ti ratio in $Ba(Zr_xTi_{1-x})O_3$ ceramics [26]

Nanakorn, et al. [21] investigated the effect of zirconium content and temperature on the *P-E* hysteresis loop of $Ba(Zr_xTi_{1-x})O_3$ ceramics with $0.00 \leq x \leq 0.08$. The report demonstrated that the loop altitude of the *P–E* hysteresis loops decreased with an increase in temperature when the temperature was raised and approached the Curie point (Figure 27). The variable of saturated polarization, remanent polarization and coercive field due to changing in zirconium content were listed in Table 3.

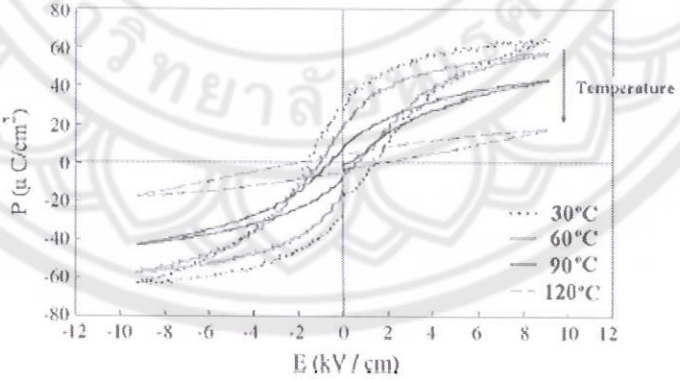

Figure 27 *P-E* hysteresis loop at the temperatures ranging from 30 °C to 120 °C of $BaZr_xTi_{1-x}O_3$ with $x = 0.08$ sintered at 1400 °C [21]

Table 3 The saturated polarization (P_s), remanent polarization (P_r), and coercive field (E_c) of BZT ceramics at 30 °C[21]

$Ba(Zr_xTi_{1-x})O_3$	P_s ($\mu C/cm^2$)	P_r ($\mu C/cm^2$)	E_c (kV/cm)
$x = 0.00$	35.862	4.424	0.696
$x = 0.02$	12.324	2.143	0.912
$x = 0.05$	57.920	25.033	1.048
$x = 0.08$	63.320	29.451	1.344

Bismuth sodium titanate ($Bi_{0.5}Na_{0.5}TiO_3$, BNT)

Bismuth sodium titanate ($Bi_{0.5}Na_{0.5}TiO_3$, BNT) was discovered by Smolensky, et al. in 1960 [33]. In pure BNT, half of all A-site positions are placed by bismuth (3^+) ions and the other half with sodium (1^+) ions. The B-site positions are placed by titanium (4^+) ions. Even though bismuth and sodium have very different charges, there is only a short range ordering of the A-site ions [34-36].

Pure BNT is a rhombohedral ferroelectric at room temperature. The rhombohedral-tetragonal phase transition temperature and Curie temperature are 300 and 540 °C, respectively [37]. The curves of permittivity versus temperature of BNT display a very interesting hump anomaly around 185 °C. This temperature is called the depolarization temperature (T_d), which corresponds to the transition from a ferroelectric to an anti-ferroelectric state. The maximum permittivity occurs around 340 °C, which is defined as T_m [36]. However, the phase transition behaviors at T_d and T_m are complicated and are not yet fully understood [37, 38].

BNT is one of the most important lead-free piezoelectric materials with a perovskite structure because of its high ferroelectricity ($P_r = 38\ \mu C/cm^2$) [32]. However, pure BNT piezoelectric ceramics are difficult to pole because of their relatively large coercive field (E_c = 73 kV/cm) and high electrical conductivity. It for this reason that ways to improve the production of pure BNT have been extensively studied.

Several techniques for improvement of BNT properties

1. Cation substituted BNT perovskite lattices

Yang, et al. [39] mentioned BKT doped to BNT for 16-20 mol% induce the morphotopic phase boundary (MPB) between rhombohedral–tetragonal, which enhanced the electrical properties of BNT. Thus, this group was investigated to discover the effects of $Bi_{0.5}K_{0.5}TiO_3$ (BKT) content on the phase structure, microstructure, dielectric and piezoelectric properties of BNT-xBKT ceramics with $0.1 \leq x \leq 0.2$. The samples were prepared via the solid-state reaction method, which were calcined and sintered at 850 °C and 1150-1200 °C, respectively. The crystal structure was studied using XRD pattern as shown in Figure 28.

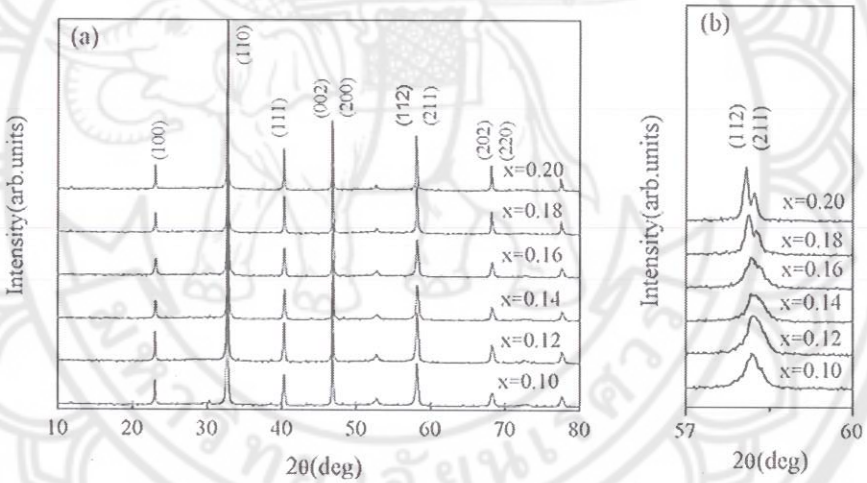

Figure 28 XRD patterns of BNT-xBKT powders [39]

From the XRD results, it can be clearly seen that the single peak of (211) at 2θ of 57° - 60° can be detected when $x < 0.16$. This suggests that the samples exhibit a rhombohedral structure. When $x = 0.16$, the diffraction peak begins to split. The (211) peak splits out to (211), (112), which indicates that the crystal was transformed to a tetragonal phase when $x = 0.18$ and 0.20. It can be concluded that the MPB is located at $0.16 \leq x \leq 0.20$. The results of the piezoelectric constant (d_{33}), electromechanical coupling factor (K_p), dielectric constant at room temperature (ε_r) and tanδ as a function of BKT content are shown in Figure 29. The results suggest that the electrical

properties of BNT-xBKT ceramics tended to enhance by the increasing of x. The maximums of d_{33} and K_p were obtained at x = 0.18 with the values of 144 pC/N and 0.29, respectively. This is because this composition is located near the MPB region.

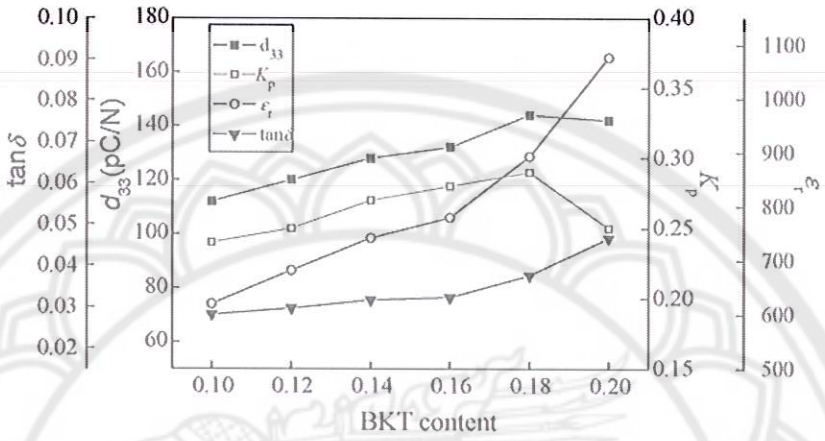

Figure 29 The piezoelectric constant d_{33}, electromechanical coupling factor K_p, dielectric constant at room temperature ε_r and tanδ as a function of BKT content [39]

Figure 30 shows the temperature dependence of ε_r and tanδ of BNT-xBKT ceramics measured at 1 kHz. There are two abnormal dielectric peaks in all samples with different compositions. The appearance of the first peak at T_t is caused when the phase is transformed from rhombohedral ferroelectric to tetragonal anti-ferroelectric. The appearance of the second peak at T_c can be explained by the transition from a tetragonal anti-ferroelectric to cubic paraelectric phase. It can be observed that the T_t shifts to lower temperature regions and the T_c shifts to higher temperature regions with increasing BKT content.

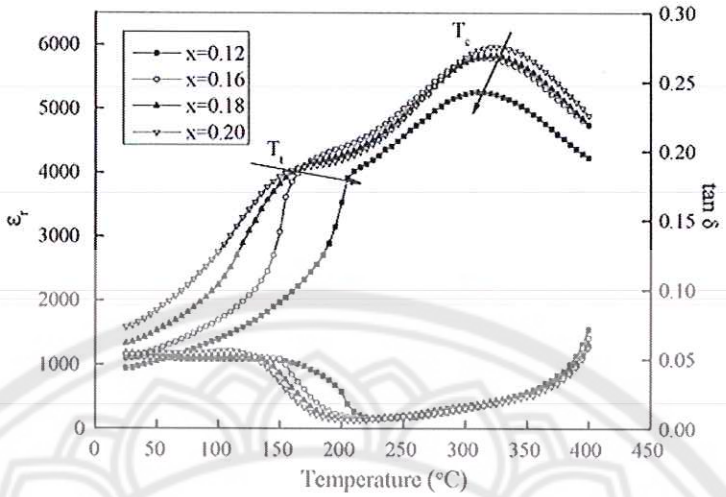

Figure 30 The temperature dependence of ε_r and tanδ of BNT-*x*BKT ceramics with different compositions [39]

The other some cation substituted to the A-site of BNT ceramics to improve BNT properties was the Li^{1+} ion. Lu, et al. [6] investigated the effects of Li and K being substituted in a BNT solid solution and recorded the effects on the crystal structure, dielectric properties and piezoelectric properties. The XRD patterns of the Li and K substituted BNT samples in the 2θ range of 20–70° and 38–50° are shown in Figure 31.

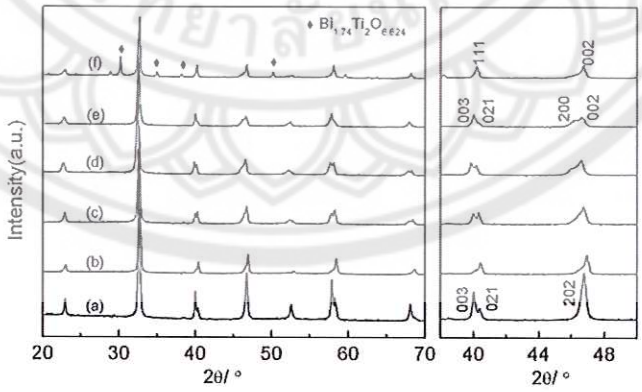

Figure 31 XRD patterns of Li and K substituted BNT ceramics; (a) BNT, (b) BNLT10, (c) BNKT10, (d) BNKT16, (e) BNKLT16-10 and (f) BNKLT16-35, in the 2θ range of 20–70° and 38–50°[6]

Generally, the symmetry of BNT at room temperature is a rhombohedral structure. This can be characterized by the splitting of (003)/(021) peaks at around 2θ of 40° and a single peak of (202) at around 2θ of 46.5°. $Bi_{0.5}K_{0.5}TiO_3$ is a perovskite type structure with tetragonal symmetry at room temperature which is characterized by the splitting of the (002)/(200) diffraction peaks at 2θ of 46.5°. The study results indicated that BNT, BNLT10 and BNKT10 have the same structure with a rhombohedral symmetry. The BNKT16 and BNKLT16-10 show the coexistence phases of a rhombohedral-tetragonal structure. With a further increase of Li content, the BNKLT16-35 shows a cubic structure and is accompanied with a secondary phase of $Bi_{1.74}Ti_2O_{6.624}$.

Figure 32 shows the temperature dependences of permittivity for Li and/or K substituted BNT ceramics at a frequency of 10 kHz. The permittivity of K doped BNT (BNKT16) ceramics is larger than that of BNT in the range of measurement temperature, especially the maximum permittivity. For Li doped BNT (BNLT10) ceramics, the permittivity is similar to pure BNT but is less than that of BNT when the temperature is higher than 200 °C. Moreover, the permittivity of K and Li doped BNT (BNKLT16-10) ceramics shows the mixing characteristics of K and Li doped BNT.

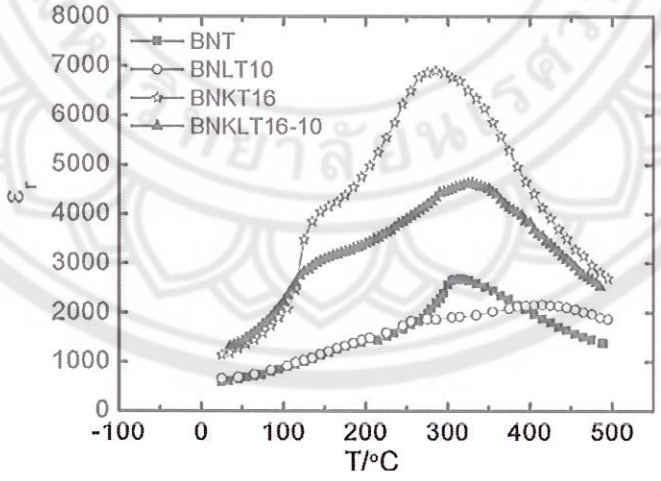

Figure 32 Temperature dependences of permittivity for Li and K substituted BNT ceramics at a frequency of 10 kHz [6]

The dielectric and piezoelectric properties of typical compositions of Li and K substituted BNT ceramics at room temperature are shown in Table 4. Li and/or K replacement for Na in BNT are improve the dielectric and piezoelectric properties, especially for the BNKLT1610 (near MPB) composition.

Table 4 Room-temperature dielectric and piezoelectric properties of BNT-based ceramics [6]

Compositions	BNT	BNLT10	BNKT10	BNKT16	BNKLT16-10
Piezoelectric constant d_{33} (pC/N)	78	95	105	138	160
Electromechanical coupling coefficient (k_p)	0.16	0.18	0.25	0.30	0.35
Dielectric permittivity ε_r at 25°C, 1 kHz	420	480	521	1020	1080
Dielectric loss $\tan\delta$ at 25°C, 1 kHz	0.03	0.036	0.023	0.029	0.038
Depolarization temperature, T_d (°C)	205	245	175	135	125
Curie temperature, T_C (°C)	315	365	285	295	335

2. Binary system of BNT-based

Chu, et al. [40] attempted to improve the electrical properties of BNT by investigating the MPB composition of the BNT-BT binary system. $(1-x)Na_{0.5}Bi_{0.5}TiO_3$–$xBaTiO_3$ with x = 0.02, 0.04, 0.06, 0.08 and 0.10 (abbreviated as NBBTx, x = 2, 4, 6, 8 and 10) were prepared via the conventional method. The X-ray diffraction patterns of the prepared samples are shown in Figure 33.

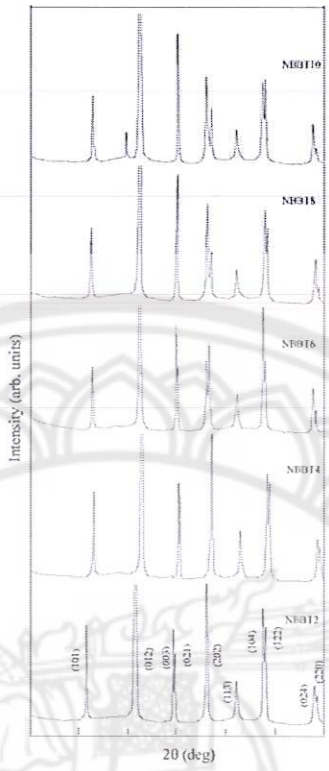

Figure 33 X-ray diffraction patterns of (1-x)$Na_{0.5}Bi_{0.5}TiO_3$–$xBaTiO_3$ ceramics [40]

At room temperature, the crystal structure of BNT is rhombohedral and that of BT is tetragonal. The X-ray diffraction revealed that NBBT2 and NBBT4 ceramics were in a rhombohedral phase. With increasing amount of $BaTiO_3$, the structures of NBBT8 and NBBT10 ceramics turned into a tetragonal symmetry characterized by (003) and (021) peaks combining into one peak and (202) peak splitting. The NBBT6 ceramics feature both rhombohedral and tetragonal symmetry. Therefore the MPB of (1-x)$Na_{0.5}Bi_{0.5}TiO_3$–$xBaTiO_3$ system is near $x = 0.06$.

The detailed electrical properties of NBBTx ceramics are shown in Table 5. The electrical properties of the (1-x)$Na_{0.5}Bi_{0.5}TiO_3$–$xBaTiO_3$ system, such as electromechanical coupling coefficient, piezoelectric constant and dielectric constant vary with the amount of $BaTiO_3$ and suggests that NBBT6 is the MPB composition.

Table 5 Electrical properties of (1-x)$Na_{0.5}Bi_{0.5}TiO_3$–$xBaTiO_3$ or NBBTx ceramics [40]

Property		Materials				
		NBBT2	NBBT4	NBBT6	NBBT8	NBBT10
Coupling factor	k_1	0.46	0.45	0.40	0.42	0.41
	k_p	0.20	0.21	0.29	0.13	0.14
Piezoelectric constant	d_{33}	78	87	122	112	94
Dielectric constant	ε^T_{33}	402	445	601	841	764
Frequency constant (Hz.m)	N_p	3190	3000	3000	2950	2980
	N_t	2680	2570	2522	2375	2418
Poisson ratio	σ	0.26	0.25	0.25	0.25	0.24
Dielectric loss	tgδ	0.0173	0.0207	0.0179	0.0204	0.0239
Maximum temperature of ε (°C)	T_m	265	230	225	250	180
Depolarization temperature (°C)	T_d	180	165	100	140	170
Remnant polarization(μC/cm²)	P_r	37	-	40	36	22.5
Corecive field (V/mm)	E_c	4700	-	2880	3200	2880

Peng, et al. [41] studied the $(Bi_{0.5}Na_{0.5})TiO_3$ (BNT)-$Ba(Zr_{0.05}Ti_{0.95})O_3$ (BZT) binary system for (1-x)BNT–BZT100x with $x \leq 0.12$. The investigation focused on searching for MPB composition between BNT (rhombohedral) and BZT (tetragonal).

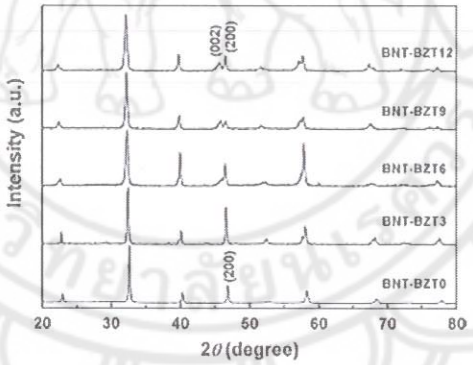

Figure 34 XRD patterns of BNT-BZT100x ceramics [41]

The X-ray diffraction patterns of BNT-BZT100x are shown in Figure 34. The splitting of (002)/(200) peaks from the single (200) peak showed that the crystal structure is transformed from rhombohedral to tetragonal due to an increase of BZT content. Moreover, the diffraction pattern of BNT-BZT9 suggested this has a MPB composition.

The $P-E$ hysteresis loops of the BNT-BZT ceramics a room temperature are shown in Figure 35. The results indicated that the BZT content highly influences the

ferroelectric properties of the system. The highest remanent polarization was exhibited in the BNT-BZT9 composition and it was near the MPB region

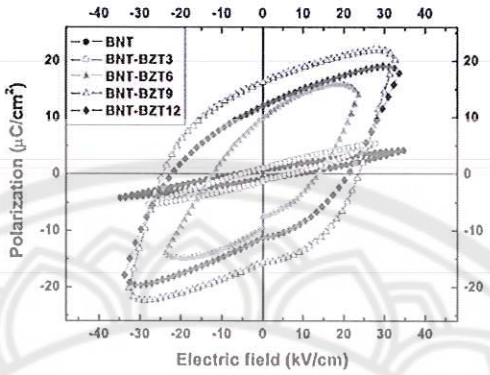

Figure 35 *P-E* loops of BNT–BZT100*x* ceramics with a maximum field of 40 kV/cm at room temperature [41]

The piezoelectric constant (d_{33}) and dielectric constant ($\varepsilon_{33}^{T}/\varepsilon_0$) of BNT–BZT ceramics altered with BZT fraction are listed in Table 6. The piezoelectric constant (d_{33}) increases with an increased BZT fraction up to 9 mol% and then decreases. The dielectric constant changes as a function of composition similarly to the piezoelectric constant, with a maximum value of 881.4 at 9 mol% BZT. The XRD pattern, piezoelectric and dielectric properties results support that BNT-BZT9 has a rhombohedral-tetragonal phase near the morphotropic phase boundary MPB.

Table 6 Piezoelectric, dielectric properties and density of BNT–BZT100*x* ceramics [41]

	d_{33} (pC/N)	T_c (°C)	ρ (g/cm^3)	$\varepsilon_{33}^{T}/\varepsilon_0$	tan δ (%)
BNT	64	310	5.32	302.6	1.752
BNT-BZT3	79	236	5.76	345.6	1.765
BNT-BZT6	107	236	5.72	844.6	2.185
BNT-BZT9	147	244	5.82	881.4	2.636
BNT-BZT12	112	259	5.69	788.7	2.980

Investigation of the combustion technique for synthesizing ferroelectric materials

1. Typical organic compound selection as fuel

Hwang, et al. [12] investigated preparation of electronic ceramic oxide powders through the combustion technique. The organic compounds (e.g., glycine, urea, citric acid, alanine, or carbohydrazide) were mixed directly with the raw materials to synthesize $Ni_{0.5}Zn_{0.5}Fe_2O_4$ powders. Some of the properties of the five selected fuel types (alanine, glycine, carbohydrazine, urea, and citric acid) are listed in the Table 7.

Table 7 Some properties of organic compounds [12]

Properties	Organic component				
	Alanine	Glycine	Carbohydrazide	Urea	Citric acid
Structural formula				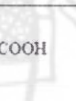	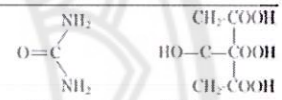
Molecular weight (g/mol)	80.1	90.1	75.1	60.1	192.1
Heat of combustion (kJ/g)	18.2	13.0	12.6	10.5	10.2
Decomposition temperature (°C)	314	262	153	135	175

The raw materials and organic fuel were mixed together in an equivalent stoichiometric ratio. The thermogravimetric analysis (TGA) of the precursor was investigated and is illustrated in Figure 36. Some organic fuels such as chabohydrazide and glycine showed that the slope of the weight loss–temperature curve was very steep. This indicated that the decomposition reaction of the fuel took place very rapidly. In case of citric acid, a distinct of three-stage weight loss was observed. When compared with other organic fuels, the slope of this curve is relatively flat which indicated that the reaction is more moderate. The analytical results obtained from synthesizing Ni–Zn ferrite products using various organic fuels is listed in Table 8. The results demonstrated that the combustion technique produces nanocrystalline and good chemically homogeneitic powders.

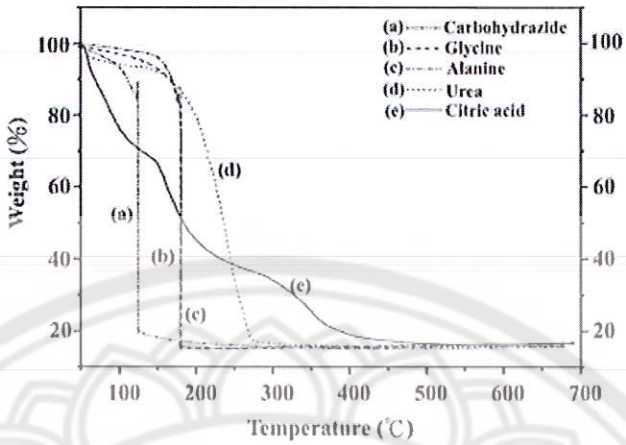

Figure 36 Typical TGA plots of the precursors prepared by using various fuels [12]

Table 8 Effects of various organic compounds and particular properties of Ni–Zn ferrite synthesized by the proposed combustion synthesis method [12]

Fuel	T_m[a] (°C)	Amount of gas produced (mole)	Crystallite size[b] (nm)	Surface area (m^2/g)	Carbon content (wt.%)	Ni^{2+}:Zn^{2+}:Fe^{3+} (molar ratio)	M_1[c] (Am^2/kg)
Alanine	1245	20.7	38.6	24.7	1.64	0.500:0.467:1.920	60.8
Glycine	1150	26.2	32.7	31.2	1.53	0.500:0.471:1.922	62.4
Carbohydrazide	1380	24.0	43.7	20.6	1.87	0.500:0.462:1.917	58.5
Urea	785	30.7	20.2	48.5	3.82	0.500:0.483:1.936	57.2
Citric acid	725	26.2	22.7	44.1	5.75	0.500:0.490:1.947	55.8

2. Decomposition reaction of the typical fuel (urea)

Eichelbaum, et al. [42] studied the decomposition reaction of urea using simultaneous thermogravimetric (TG), differential thermal analysis (DTA) and measured the gasses produce. The results are shown in Figure 37.

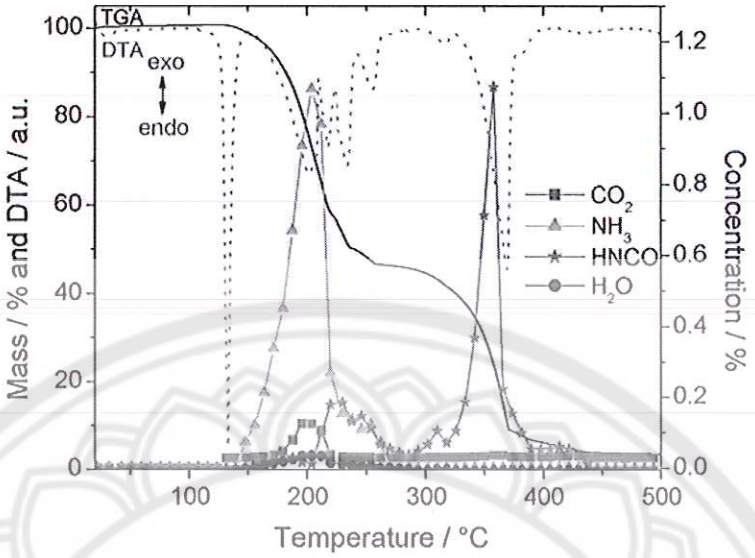

Figure 37 TGA, DTA graphs and quantitative results of the GC/MS evolved gas analysis [42]

The results revealed that the decomposition reactions of urea show multi-stages. Urea initially melted at 133 °C and then several decomposition reactions occurred between 150-250 °C. The main reaction consisted of the thermolysis of urea to ammonia (NH_3) and isocyanic acid (HNCO). However, only a minor amount of HNCO was detected between 210 and 270 °C. The weak production of CO_2 at 200 °C can be explained by the hydrolysis of HNCO with trace water in the original sample to NH_3 as shown in Figure 38(a). The other main reactions in this temperature range were the formation of ammelide. This started with the reaction between HNCO and urea to form biuret at a temperature higher than 150 °C and then the biuret reacted with HNCO to form ammelide as shown in Figure 38(b). Above 270 °C, cyanuric acid was formed from HNCO (Figure 38(c)). A large mass loss can be observed in the TGA spectrum (Figure 37) accompanied with a sharp endothermic peak at 370 °C and the production of large amounts of HNCO. This can be explained by the thermolysis of cyanuric acid, which decomposes above 300 °C (Figure 38(c)). At the same time, ammelide reacted with NH_3 and ammeline was formed at temperature higher than 270 °C (Figure 38(d)). Thereafter, the ammeline continuously decomposed to HNCO and cyanogens (CN_2) at high temperature as shown in Figure 38(e).

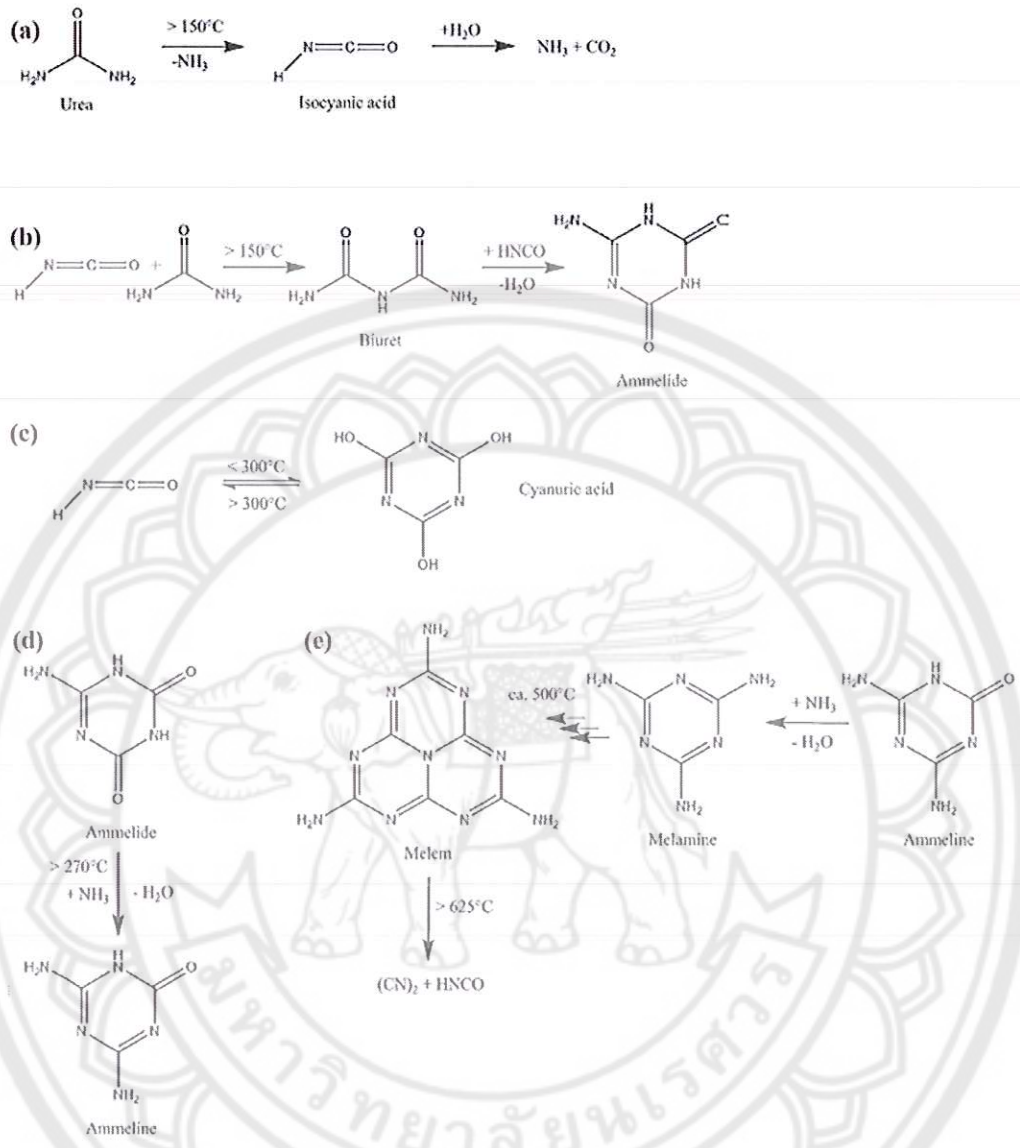

Figure 38 Schematic diagram of major decomposition reaction of urea [42]

3. Fuel content selection

The decomposition reactions of the organic compounds released high energy in multi-stages. Some research groups studied the synthesis of electroceramics with organic compound added, and expected the released energy from the decomposition reaction of fuel to be helpful in accelerating the chemical reaction of the raw materials [41-44]. Moreover, Hwang, et al. [12] suggested that the NH_3 released from the decomposition of organic compounds such as urea, glycine, alanine and citric acid could react with NO_x from the decomposed metal nitrate. The oxidation-reduction

reaction is shown in Eq.16. The energy released from this oxidation-reduction reaction accelerated the chemical reaction of raw materials.

$$4x\mathrm{NH_3} + 10\mathrm{NO}_x \rightarrow (5+2x)\mathrm{N_2} + 6x\mathrm{H_2O} + 2x\mathrm{O_2} \qquad \text{[Eq.16]}$$

There are two main energy releases during electroceramic synthesis in which the added raw materials consist of metal nitrate and organic compound. The first main energy is released from the decomposition reaction of fuel and the next one is released from the oxidation-reduction reaction between ammonia (decomposed from amine group of fuel) and NO_x (decomposed from metal nitrate of raw materials). This released energy helps to speed up the chemical reaction of the raw materials. However, it has been reported that an exothermic redox reaction (oxidation and reduction reaction taking place simultaneously) could be initiated only when the oxidizer and the fuel are mixed intimately in a fixed proportion. The basis of the combustion synthesis process is derived from the thermochemical concepts used in propellant chemistry [43-48].

The ratio of the oxidizer and fuel for the redox mixture is calculated using the equivalence ratio (φ), defined as

$$\varphi = \frac{O}{F} \qquad \text{[Eq.17]}$$

Where (O) is the total oxidizing valence and (F) the total reducing valence of the elements present in the mixture [32]. According to propellant theory, the species M^{2+}, M^{3+}, M^{4+}, C and H are considered to be reducing with valencies of + 2, + 3,+ 4, + 4 and + 1 respectively. Oxygen is considered to be an oxidizing species with valence - 2 and nitrogen is considered to be valence neutral with a value of zero. Where the φ value is equal to unity (stoichiometric), the released energy reaches its maximum [43]. A mixture is fuel rich if $\varphi < 1$, fuel lean if $\varphi > 1$ [43].

Chavan, et al. [46] investigated the effects of oxidant-to-fuel ratio on the properties of Y_2O_3 synthesizing. The raw materials of $Y(NO_3)_3 \cdot 6H_2O$ and glycine (selected fuel) were mixed by the molar concentration in which the oxidant (yttrium nitrate) was kept constant at unity and the fuel concentration was varied. The elemental stoichiometric coefficient φ which is the ratio between the total valencies

of fuel (glycine; NH_2CH_2COOH) and that of the oxidizer (yttrium nitrate), can be calculated as shown below

$$\varphi = \frac{0_{(N)} + 2\times 1_{(H)} + 4_{(C)} + 2\times 1_{(H)} + 4_{(C)} - 2_{(O)} - 2_{(O)} + 1_{(H)}}{3_{(Y)} + 3\times 0_{(N)} + 9\times -2_{(O)}} \qquad \text{[Eq.18]}$$

In the present system, to satisfy this stoichiometric ratio the yttrium nitrate (oxidizing valency = 15−) to glycine (reducing valency = 9+) molar ratio was found to be 1:1.66. Previously the properties of powders had been studied by varying the molar ratios on either side of this ratio, i.e., fuel-lean compositions as 1:0.5, 1:1.0 and fuel rich i.e., 1:2.0, 1:2.5, 1:3.

Table 4 shows some properties of prepared powders with various oxidants to fuel ratio. The smallest crystallite size (8 nm) and the highest surface area (165 m^2/gm) were observed for the powder with a lean fuel condition (1:1.0). The powder with a stoichiometric composition had the largest crystallite size (30 nm) and the lowest surface area (57 m^2/gm). Thus the product with the best powder properties was the one from the lean fuel precursor, with an oxidant-to-fuel ratio of 1:1.0. These results could be attributed to two competing effects. The first one is the enthalpy of the reaction and the next is the subsequent flame temperatures associated with it and the number of moles of gaseous product evolved during combustion.

For the stoichiometric composition (1:1.66), which is a composition corresponding to the principle of propellant chemistry, the highest flame temperature observed (1440 °C) lead to large crystallites and a low surface area. Moreover, high temperature affects the prepared powders exhibited local partial sintering particle characteristics.

Increasing to a rich fuel composition (1:2.0, 1:2.5 and 1:3.0) decreased the flame temperature and there was no flame in the 1:3.0 composition. This was probably due to the lack of sufficient oxidant required for the complete combustion of the excess fuel. Moreover, increasing the fuel ratio caused the number of moles of gases released to also increase. These liberated gases dissipated the heat of combustion and limited the temperature rising, thus reducing the possibility of premature local partial sintering among the primary particles [46].

Table 9 Comparison of powder properties with different oxidant-to-fuel ratio [45]

Powders	O/F	Flame temperature (°C)	No. of moles of gases as per equation	Crystalline size (nm)	Surface area (m^2/g)	Sintered density (%)
a	1:0.5	No flame	11.88	12	44	-
b	1:1.0	No flame	13.00	8	165	97
c	1:1.66	1440	15.42	30	57	92
d	1:2.0	1200	17.50	25	147	94
e	1:2.5	1050	20.00	9	114	96
f	1:3.0	No flame	22.50	9	90	94

CHAPTER IV

PHASE FORMATION, MICROSTRUCTURE AND DIELECTRIC PROPERTIES OF $Bi_{0.5}(Na_{0.74}K_{0.16}Li_{0.10})_{0.5}TiO_3$-$Ba(Zr_{0.5}Ti_{0.95})O_3$ CERAMICS PREPARED VIA THE COMBUSTION TECHNIQUE

Introduction

It is well known that BNT is a ferroelectric ceramic which possesses strong ferroelectricity [49]. However, the application for electronic devices of this material is limited by some problems such as its high coercive field, low piezoelectricity and low dielectric constant [11]. Therefore, other compositions or some cation additives were also added into BNT to improve their characteristics [50, 51]

Yang, et al. [52] modified BNT by substituting Na^+ by K^+ for 10-20 mol%. The result demonstrated that K-substitution induced the MPB region between rhombohedral–tetragonal phases at 18 mol% of K. This composition is very promising lead-free piezoelectric materials because it shows the optimum values of d_{33}, K_p, ε_r and tanδ of 144 pC/N, 0.29, 893 and 0.037, respectively. Lu, et al. [6] investigated the K^{1+} and Li^{1+} ion additive by replacing the Na^{1+} ion to form a BNKLT system. The study results suggested that the $Bi_{0.5}(Na_{0.74}K_{0.16}Li_{0.10})_{0.5}TiO_3$ or BNKL1610 composition showed the coexistence of a rhombohedral and tetragonal structure which is the MPB composition. The MPB composition led to a great enhancement in electrical properties compared with BNT. There was an increasing of d_{33} from 78 to 160 pC/N, an increasing of K_p from 0.16 to 0.35 and an increasing of ε_r from 420 to 1080. On the other view point, many researchers have reported BNT- improvement by introducing into the BNT-binary or ternary system chemical compositions such as BNT-BZT [9, 10], BNT-KNN [8] or BNT-BKT-BF [53, 54]. For example, Parija *et al.* [11] demonstrated doping BZT to BNT enhanced the ε_m from 1020 to 3533, d_{33} from 41 to 131 pC/N and P_r from 2.5 to 12 μC/cm^2 for 5 mol% BZT doped.

Recently, the idea of combining cation additives and the binary system of BNT-based solid solution to improve BNT properties has generated interest. Jarupoom, et al. [55] produced a system of (1-*x*)BNLT-*x*BT where 1.7 mol% La^{3+}

doped BNT and $0 \leq x \leq 0.10$. The ε_r and ε_{max} values of the BNLT–BT system were enhanced by the addition of BT fraction while T_c was lowered. Moreover, BT doping helped to reduce the tanδ of the ceramics at high temperature. The ε_r and ε_{max} showed maximum values of 1,615 and 4250 obtained from the BNLT with an addition of 10 mol% BZT.

The objective of this work is to investigate the possibilities of improving BNT properties by producing a new system of (1-*x*)BNKLT1610-*x*BZT5 or BNKLT-100*x*BZT ceramics. The effects of BZT fraction on phase formation, morphology and dielectric properties were also investigated. The samples were also synthesized through the combustion technique since this route has been shown an effective way to improve BNT and BZT properties [56-58].

Experimental procedure

The (1-*x*)BNKLT1610-*x*BZT5 ($x = 0.025 \leq x \leq 0.15$, step = 0.025) ceramics were synthesized using the combustion technique. Highly pure bismuth oxide (Bi_2O_3), sodium carbonate (Na_2CO_3), potassium carbonate (K_2CO_3), lithium carbonate (Li_2CO_3), titanium oxide (TiO_2), barium carbonate ($BaCO_3$) and zirconium dioxide (ZrO_2) were used as starting materials. Firstly, the raw materials were weighed according to the designed chemical formulae and were ball milled in an ethanol medium for 24 h. After being mixed with CH_4N_2O (fuel), the $Bi_{0.5}(Na_{0.74}K_{0.16}Li_{0.10})_{0.5}TiO_3$ (BNKLT1610) and $Ba(Zr_{0.05}Ti_{0.95})O_3$ (BZT5) were synthesized at 750 °C for 2 h and 1000 °C for 5 h, respectively. After calcination, the two synthesized powders were mixed with different values of *x*, milled once again, dried, and granulated by adding PVA. The granulated powders were pressed into disks of 15 mm diameter and then pressed using a uniaxial pressure of 80 MPa. These disks were sintered in air at 1100 °C for 2 h. The crystal structures of the ceramics were characterized by an X-ray diffractometer. The scanning electron microscopy (SEM) was employed to examine the microstructure of the sintered ceramics. The sintered disks were polished and had silver paste applied to both surfaces to measure their electrical properties. After applying the silver, the disks were fired at 600 °C for 5 min and the temperature dependences of the dielectric properties were measured using a LCR meter.

Results and discussion

The X-ray diffraction patterns of the BNKLT-100*x*BZT ceramics with $0 \leq x \leq 0.15$ are shown in Figure 39. All of the BNKLT-BZT samples showed a pure perovskite phase which indicated that the BZT had completely diffused into the lattice to form a solid solution. Moreover, the diffraction peaks at 2θ of 44-48° at a very low scanning rate (step size 0.00116°, time/θ 7.42 s, and scan speed 0.05152°/s) showed interesting characteristics due to a significant change in the composition (Figure 39(b)). The investigation demonstrated that there are two features of diffraction patterns of interest. First, the diffraction peaks shifted to a lower angle when the BZT content increased. This suggested that the unit cells were stretched, which may be because the larger size Ba^{2+} (161 pm) occupies the A-site lattice by replacing Bi^{3+} (130 pm) and/or because the Na^{1+} (139 pm) and Zr^{4+} (72 pm) ion replaces the Ti^{4+} (61 pm) ion at the B-site lattice. The next diffraction feature of interest is the splitting of the (002) and (200) peaks. For BNKLT ceramics, the result of XRD patterns in the previous chapter demonstrated the coexistence of rhombohedral and tetragonal phases where the rhombohedral phase dominated. Additional BZT into BNKLT for BNKLT-2.5BZT induced an occurrence of a small hump at the left side of the (200) peak, indicating that the crystal structure was initially transformed to a tetragonal phase. The asymmetrical feature was distinctly observed when the BZT content was increased to 5 mol%. For BNKLT-7.5BZT composition, the diffraction peak appeared to split to (200) and (002) peaks. The splitting characteristic clearly observed when the BZT content was increased, which indicated that the tetragonallity tended to increase.

To understand the variation of unit cell volume due to a change in composition, the lattice parameters were also investigated. From the previous chapter, the BNKLT was assumed as a rhombohedral structure and the lattice parameter *a* was calculated. For BNKLT-BZT structure, the splitting of (002) and (200) peaks at 2θ of 44-48° was observed in BZT higher containing than 5 mol%. Therefore, the crystal structure of BNKLT-*x*BZT was assumed to be a rhombohedral and tetragonal structure for $x \leq 5$ mol% and $x > 5$ mol%, respectively. The lattice parameters, unit cell volume and *c*/*a* ratio were calculated and are listed in Table 10. The calculation for the lattice parameters was based on different structures. The calculated lattice parameter *a*

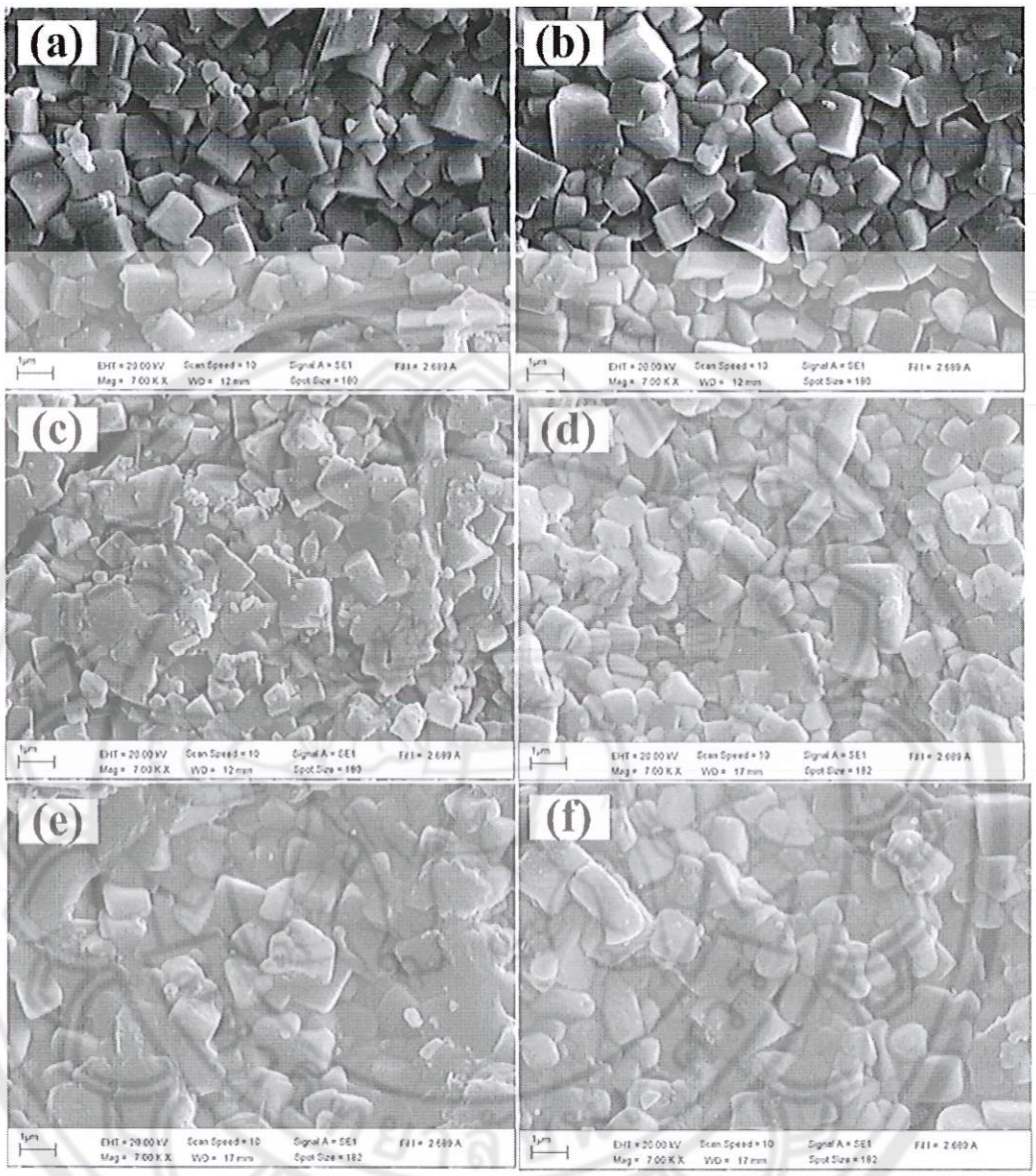

Figure 40 SEM photographs of surface of BNKLT-100*x*BZT ceramics; (a) $x = 0.025$, (b) $x = 0.050$, (c) $x = 0.075$, (d) $x = 0.100$, (e) $x = 0.125$ and (f) $x = 0.150$

Table 10 The lattice parameters *a* and *c*, unit cell volume, *c/a* ratio and average grain size of BNKLT-100*x*BZT ceramics

Samples	Lattice parameters		Unit cell Volume	*c/a* ratio	Average grain size
	a (Å)	*c* (Å)	(Å^3)		(μm)
BNKLT	3.432	-	-	-	1.72
BNKLT-2.5BZT	3.438	-	-	-	1.64
BNKLT-5.0BZT	3.449	-	-	-	1.89
BNKLT-7.5BZT	3.916	3.971	61.740	1.014	1.70
BNKLT-10.0BZT	3.926	3.986	62.368	1.015	1.43
BNKLT-12.5BZT	3.928	3.988	62.453	1.015	1.59
BNKLT-15.0BZT	3.927	3.991	62.560	1.016	1.44

The measured density with a variation in BZT content of BNKLT-100*x*BZTBZT is listed in Table 11. The density of the ceramics was in the range of 5.73–5.87 g/cm^3. The highest density was exhibited in BNKLT-12.5BZT. It can be observed that high density ceramics were obtained from the samples with high BZT content. In the previous chapter, the results indicated Bi and/or K and/or Na ions evaporate during the sintering process. This caused resulted in less dense samples. By the addition of BZT, evaporated ions can be substituted by more stable ions such as Na, and the volatility is reduced [58]. Therefore, the relative density is enhanced.

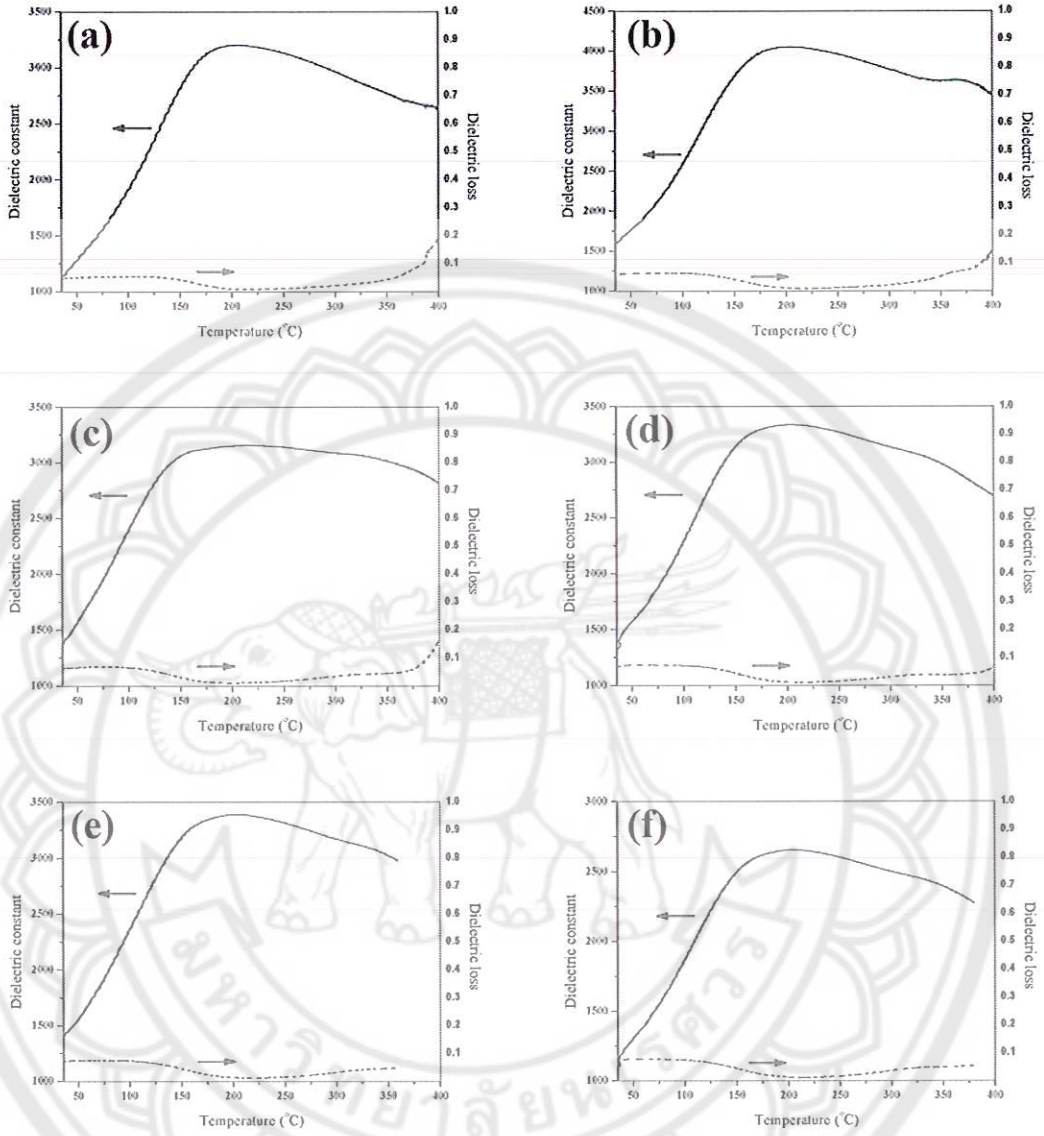

Figure 41 Temperature dependence of dielectric constant and dielectric loss of the BNKLT-*x*BZT ceramics with $0.025 \leq x \leq 0.15$

The dielectric constant and loss as a function of temperature for BNKLT-100*x*BZT ceramics is illustrated in Figure 41. For the sample with 2.5 mol% BZT (Figure 41(a)), the distinct dielectric peak with maximum value of dielectric constant occurs at ~200 °C. This point is referred to the dielectric peak in which the phase transition from a ferroelectric to an anti-ferroelectric phase at temperature called T_d. The dielectric curve shows an initial occurrence of another dielectric peak at a higher temperature (~360 °C). This point is clearly observed from the dielectric loss curve

and this point is referred to the dielectric peak in which the phase transition from anti-ferroelectric to paraelectric phase at temperature is called T_m. By increasing of BZT content to 5 mol%, the dielectric loss peak at T_m is more observed and shifted to a lower temperature (Figure 41(b)). The shifting of the dielectric loss peak at T_m tended move toward a lower temperature as the BZT content increased (Figure 41(c)-(f)). Increasing the BZT content only slightly affected the dielectric loss peak at T_d. However, the dielectric constant and dielectric loss could not be measured at high temperatures for BNKLT with 12.5 and 15 mol% BZT due to the dielectric constant and dielectric loss which was found to decrease and increase dramatically, respectively. This indicated that the materials exhibit high conductivity at high temperature, because the structure changed to paraelecric above Curie temperature [53]. The T_d, T_m, maximum dielectric constant (ε_{max}), dielectric constant at room temperature (ε_r) and dielectric loss at room temperature (tanδ) were observed and are listed in Table 11.

It can be noted that, an increase of BZT content caused the T_m to shift to a lower temperature. This is because the BZT has a lower value of paraelectric-phase transition temperature (~100 ^{o}C) [59] compared with that of BNKLT (~335 ^{o}C) [6]). In term of dielectric constant, the maximum dielectric constant was exhibited at the dielectric peak near T_d for all samples. This phenomenon shows the contrary behavior of the dielectric curve of BNT as reported in the literature [49, 60] in which the dielectric peak shows its higher altitude at T_m and its lower altitude at T_d. This can be attributed to the core-shell structure which was formed in the materials and because the shell grain was more highly influenced than the core grain as described in the previous chapter. The variation of ε_r and ε_{max} for various BZT contents are graphically presented in Figure 42. An increase of the BZT content led to both ε_r and ε_{max} to be enhanced and reach maximum values at 5 mol% BZT. Thereafter, ε_{max} suddenly dropped and then increased with an increase of BZT content until it reached 12.5% when it then decreased. Chu, et al. [40] reported that the MPB composition of BNT-BT is 6 mol% BT. Therefore, the highest values of ε_r and ε_{max} exhibited in the sample of BNKLT-5BZT may be attributed to this composition being near the MPB region of the BNKLT-BZT system. At the MPB region, the polarization vector can easily switch between all the allowed polarization orientations. Therefore, the dielectric properties

increased [61]. After dropping, ε_{max} tended to increase with increasing BZT content from 7.5 to 12.5 mol%. This result corresponds with the literature [62], which suggests that the dielectric constant of BNT-BT increase when the composition is near the tetragonal side of MPB region. However, the cause of reduction of ε_r and ε_{max} in BNKLT-15BZT sample is ambiguous.

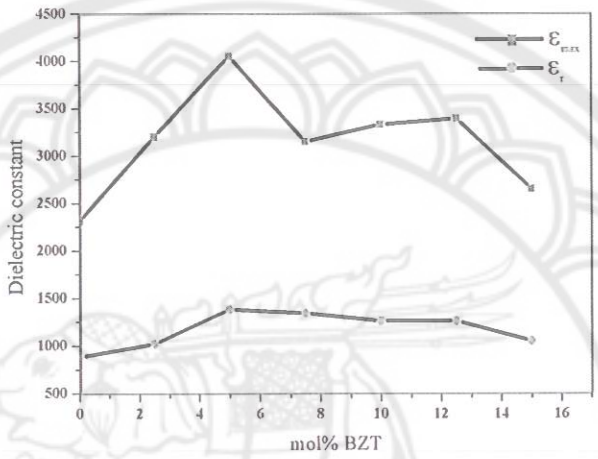

Figure 42 ε_r and ε_{max} as function of BZT fraction for BNKLT-xBZT ceramics with $0 \leq x \leq 0.15$

Table 11 Density, T_d, T_m, ε_r, ε_{max} and tanδ of BNKLT-100xBZT ceramics

Samples	density (g/cm^3)	T_d (^0C)	T_m (^0C)	ε_r	ε_{max}	tanδ at T_r
BNKLT	5.73	195	-	880	2,310	0.039
BNKLT-2.5BZT	5.81	190	-	1,020	3,200	0.045
BNKLT-5.0BZT	5.83	193	360	1,380	4,050	0.051
BNKLT-7.5BZT	5.79	191	330	1,340	3,150	0.061
BNKLT-10.0BZT	5.82	189	325	1,260	3,330	0.065
BNKLT-12.5BZT	5.87	190	320	1,260	3,390	0.068
BNKLT-15.0BZT	5.84	188	310	1,050	2,650	0.070

CHAPTER V

CONCLUSIONS

The effects of BZT content on phase formation, morphology and dielectric properties of BNKLT-100*x*BZT were studied. The XRD results demonstrated that the co-existence of the rhombohedral-tetragonal phase is exhibited for all samples. The addition of BZT content allowed the tetragonal phase to increase while the rhombohedral phase decreased. Moreover, the increase of BZT content caused the lattice parameters, unit cell volume and *c/a* ratio to increase. The SEM results suggested that the average grain size was slightly affected by the addition of BZT. However, the relative density tended to increase with increasing BZT fraction. After dielectric properties characterization had been employed, it was found that the addition of BZT caused T_m to shift to a lower temperature while T_d is insignificantly shifted. The appearance of the dielectric constant peak at T_d rather than at T_m was apparent for all compositions. This indicated that the grain shell has a higher influence than grain core in a BNKLT-BZT system. The maximum ε_r and ε_{max} with the values of 1,380 and 4,050 were observed from the sample with the composition BNKLT-5BZT. This can be attributed to the fact that this composition is located near the MPB region.

REFERENCES

[1] Kim, H. T. and Han, Y. H. (2004). Sintering of nanocrystalline $BaTiO_3$. **Ceramics International**, 30, 1719-1723.

[2] Yoshimura, M., Suchanek, W. L., Watanabe, T. and Sakurai, B. (1999). In situ fabrication of $SrTiO_3$–$BaTiO_3$ layered thin films by hydrothermal-electrochemical technique. **Journal of the European Ceramic Society,** 19, 1353-1359.

[3] Koerfer, S., De Souza, R. A., Yoo, H.I. and Martin, M. (2008). Diffusion of Sr and Zr in $BaTiO_3$ single crystals. **Solid State Sciences,** 10, 725-734.

[4] Pantou, R., Dubourdieu, C., Weiss, F., Kreisel, J., Köbernik, G. and Haessler, W. (2002). Effect of substitution of Ti by Zr in $BaTiO_3$ thin films grown by MOCVD. **Materials Science in Semiconductor Processing,** 5, 237-241.

[5] Razak, K. A., Yip, C. J. and Sreekantan, S. (2011). Synthesis of $(Bi_{0.5}Na_{0.5})TiO_3$ (BNT) and Pr doped BNT using the soft combustion technique and its properties. **Journal of Alloys and Compounds,** 509, 2936-2941.

[6] Lu, W., Wang, Y., Fan, G., Wang, X. and Liang, F. (2011). The structural and electric properties of Li- and K-substituted $Bi_{0.5}Na_{0.5}TiO_3$ ferroelectric ceramics. **Journal of Alloys and Compounds**, 509, 2738-2744.

[7] Li, H., Feng, C. and Yao, W. (2004). Some effects of different additives on dielectric and piezoelectric properties of $(Bi_{1/2}Na_{1/2})TiO_3$–$BaTiO_3$ morphotropic-phase-boundary composition. **Materials Letters,** 58, 1194-1198.

[8] Laoratanakul, P., Yimnirun, R. and Wongsaenmai, S. (2011). Phase formation and dielectric properties of bismuth sodium titanate–potassium sodium niobate ceramics. **Current Applied Physics**, 11, S161-S166.

[9] Du, P., Luo, L., Li, W., Zhang, Y. and Chen, H. (2013). Photoluminescence and piezoelectric properties of Pr-doped NBT–*x*BZT ceramics: Sensitive to structure transition. **Journal of Alloys and Compounds**, 559, 92-96.

[10] Lee, W., Lee, M., Tseng, C., Huang, Y. and Wu, C. (2009). Crystal structure and ferroelectric properties of $(Bi_{0.5}Na_{0.5})TiO_3$-$Ba(Zr_{0.05}Ti_{0.95})O_3$ piezoelectric ceramics. **Journal of the American Ceramic Society**, 92, 1069-1073.

[11] Parija, B., Badapanda, T., Rout, S. K., Cavalcante, L. S., Panigrahi, S., Longo, E., et al. (2013). Morphotropic phase boundary and electrical properties of $1-x[Bi_{0.5}Na_{0.5}]TiO_3-xBa[Zr_{0.25}Ti_{0.75}]O_3$ lead-free piezoelectric ceramics. **Ceramics International**, 39, 4877-4886.

[12] Hwang, C.-C., Wu, T.-Y., Wan, J. and Tsai, J.-S. (2004). Development of a novel combustion synthesis method for synthesizing of ceramic oxide powders. **Materials Science and Engineering: B**, 111, 49-56.

[13] Mangalaraja, R. V., Mouzon, J., Hedström, P., Kero, I., Ramam, K. V. S., Camurri, C. P., et al. (2008). Combustion synthesis of Y_2O_3 and $Yb-Y_2O_3$: Part I. Nanopowders and their characterization. **Journal of Materials Processing Technology**, 208, 415-422.

[14] Xu, J., Xue, D. and Yan, C. (2005). Chemical synthesis of $NaTaO_3$ powder at low-temperature. **Materials Letters**, 59, 2920-2922.

[15] George, C. N., Thomas, J. K., Kumar, H. P., Suresh, M. K., Kumar, V. R., Wariar, P. R. S., et al. (2009). Characterization, sintering and dielectric properties of nanocrystalline barium titanate synthesized through a modified combustion process. **Materials Characterization**, 60, 322-326.

[16] Feng, Q., Ma, X. H., Yan, Q. Z. and Ge, C. C. (2009). Preparation of soft-agglomerated nano-sized ceramic powders by sol–gel combustion process. **Materials Science and Engineering: B**, 162, 53-58.

[17] Moulson, A. J. and Herbert, J. M. (1992). **Electroceramics**. London: Chapman & Hall.

[18] Barsoum, M. W. (2003). **Fundamentals of ceramics**. London: McGraw-Hill.

[19] Haertling, G. H. (1999). Ferroelectric ceramics: history and technology. **J. Am. Ceram. Soc.**, 82, 797–818.

[20] Safari, A., Panda, R. K. and Janas, V. F. (1996). Lead-free materials. **Key Engineering Materials**, 122, 35-70.

[21] Nanakorn, N., Jalupoom, P., Vaneesorn, N. and Thanaboonsombut, A. (2008). Dielectric and ferroelectric properties of $Ba(Zr_xTi_{1-x})O_3$ ceramics. **Ceramics International**, 34, 779-782.

[22] Loehman, R. E. (2010). **Characterization of ceramics**. New York: Taylor&Francis.

[23] Dixit, A., Majumder, S. B., Dobal, P. S., Katiyar, R. S. and Bhalla, A. S. (2004). Phase transition studies of sol–gel deposited barium zirconate titanate thin films. **Thin Solid Films**, 447–448, 284-288.

[24] Kuang, S. J., Tang, X. G., Li, L. Y., Jiang, Y. P. and Liu, Q. X. (2009). Influence of Zr dopant on the dielectric properties and Curie temperatures of $Ba(Zr_xTi_{1-x})O_3$ ($0 \leq x \leq 0.12$) ceramics. **Scripta Materialia,** 61, 68-71.

[25] Ciomaga, C.E., Calderone, R., Buscaglia, M.T., Viviani, M., Buscaglia, V., Mitoseriu, L., Stancu, A. and Nanni, P. (2006) Relaxor properties of $Ba(Zr,Ti)O_3$ ceramics. **J. Optoelectron. Adv. Mater**, 8, 944–948.

[26] Chen, H., Yang, C., Fu, C., Shi, J., Zhang, J. and Leng, W. (2008). Microstructure and dielectric properties of $BaZr_xTi_{1-x}O_3$ ceramics. **J. Mater. Sci.,** 19, 379–382.

[27] Reddy, S. B., Rao, K. P. and Rao, M. S. R. (2007). Nanocrystalline barium zirconate titanate synthesized at low temperature by an aqueous co-precipitation technique. **Scripta Materialia,** 57, 591-594.

[28] Huang, H.H., Chiu, H.H.S., Wu, N.C. and Wang, M.C. (2008). Tetragonality and properties of $Ba(Zr_xTi_{1-x})O_3$ ceramics determined using the Rietveld method. **Metallurgical and Materials Transactions,** 39A, 3276–3284.

[29] Neirman, S. M. (1988). The Curie point temperature of Ba(ZrxTi1-x)O3solid solutions**. Journal of Materials Science**, 23, 3973-3980.

[30] Binhayeeniyi, N., Sukvisut, P., Thanachayanont, C. and Muensit, S. (2010). Physical and electromechanical properties of barium zirconium titanate synthesized at low-sintering temperature. **Materials Letters,** 64, 305-308

[31] Yu, Z., Ang, C., Guo, R. and Bhalla, A. S. (2007). Dielectric properties of $Ba(Zr_xTi_{1-x})O_3$solid solutions. **Materials Letters**, 61, 326-329.

[32] Xiong, J.W., Zeng, B. and Cao, W.Q. (2008). Investigation of dielectric and relaxor ferroelectric properties in $Ba(Zr_xTi_{1-x})O_3$ ceramics. **Journal of Electroceramics**, 21, 124–127.

[33] Jaita, P., Watcharapasorn, A. and Jiansirisomboon, S. (2011). Effects BNT compound incorporated on structure and electrical properties of PZT ceramic. **Current Applied Physics**, 11, S77-S81.

[34] Pookmanee, P., Rujijanagul, G., Ananta, S., Heimann, R. B. and Phanichphant, S. (2004). Effect of sintering temperature on microstructure of hydrothermally prepared bismuth sodium titanate ceramics. **Journal of the European Ceramic Society**, 24(2), 517-520.

[35] Ji, W.-J., Chen, Y.-B., Zhang, S.-T., Yang, B., Zhao, X.-N. and Wang, Q.-J. (2012). Microstructure and electric properties of lead-free $0.8Bi_{1/2}Na_{1/2}TiO_3$–$0.2Bi_{1/2}K_{1/2}TiO_3$ ceramics. **Ceramics International**, 38, 1683-1686.

[36] Chou, C.-S., Wu, C.-Y., Yang, R.-Y. and Ho, C.-Y. (2012). Preparation and characterization of the bismuth sodium titanate ($Na_{0.5}Bi_{0.5}TiO_3$) ceramic doped with ZnO. **Advanced Powder Technology**, 23, 358-365.

[37] Hiruma, Y., Yoshii, K., Nagata, H. and Takenaka, T. (2008). Phase transition temperature and electrical properties of $(Bi_{1/2}Na_{1/2})TiO_3$–$(Bi_{1/2}A_{1/2})TiO_3$ (A= Li and K) lead-free ferroelectric ceramics. **Journal of Applied Physics**, 103, 084121.

[38] Hiruma, Y., Nagata, H. and Takenaka, T. (2009). Depolarization temperature and piezoelectric properties of $(Bi_{1/2}Na_{1/2})TiO_3$–$(Bi_{1/2}Li_{1/2})TiO_3$–$(Bi_{1/2}K_{1/2})TiO_3$ lead-free piezoelectric ceramics. **Ceramics International**, 35, 117-120.

[39] Yang, Z., Liu, B., Wei, L. and Hou, Y. (2008). Structure and electrical properties of $(1\text{-}x)Bi_{0.5}Na_{0.5}TiO_3$–$xBi_{0.5}K_{0.5}TiO_3$ ceramics near morphotropic phase boundary. **Materials Research Bulletin**, 43, 81-89.

[40] Chu, B.-J., Chen, D.-R., Li, G.-R. and Yin, Q.-R. (2002). Electrical properties of $Na_{1/2}Bi_{1/2}TiO_3$–$BaTiO_3$ ceramics. **Journal of the European Ceramic Society**, 22, 2115-2121.

[41] Peng, C., Li, J.-F. and Gong, W. (2005). Preparation and properties of $(Bi_{1/2}Na_{1/2})TiO_3$–$Ba(Ti,Zr)O_3$ lead-free piezoelectric ceramics. **Materials Letters**, 59, 1576-1580.

[42] Eichelbaum, M., Farrauto, R. J. and Castaldi, M. J. (2010). The impact of urea on the performance of metal exchanged zeolites for the selective catalytic reduction of NOx: Part I. Pyrolysis and hydrolysis of urea over zeolite catalysts. **Applied Catalysis B: Environmental**, 97, 90-97.

[43] Chaiyo, N., Muanghlua, R., Niemcharoen, S., Boonchom, B. and Vittayakorn, N. (2011). Solution combustion synthesis and characterization of lead-free piezoelectric sodium niobate ($NaNbO_3$) powders. **Journal of Alloys and Compounds**, 509, 2445-2449.

[44] Pampuch, R. (1999). Advanced HT ceramic materials via solid combustion. **Journal of the European Ceramic Society**, 19, 2395-2404.

[45] Fumo, D. A., Jurado, J., Segadães, A. M. and Frade, J. R. (1997). Combustion synthesis of iron-substituted strontium titanate perovskites. **Materials Research Bulletin**, 32, 1459-1470.

[46] Chavan, S. V., Pillai, K. T. and Tyagi, A. K. (2006). Combustion synthesis of nanocrystalline yttria: Tailoring of powder properties. **Materials Science and Engineering: B**, 132, 266-271.

[47] Fumo, D. A., Morelli, M. R. and Segadães, A. M. (1996). Combustion synthesis of calcium aluminates. **Materials Research Bulletin**, 31, 1243-1255.

[48] Madhana Kumar, K. S. and John Berchmans, L. (2009). Combustion synthesis of of copper doped calcium aluminate. **Ceramics International**, 35, 1277-1280.

[49] Zuo, R., Su, S., Wu, Y., Fu, J., Wang, M. and Li, L. (2008). Influence of A-site nonstoichiometry on sintering, microstructure and electrical properties of $(Bi_{0.5}Na_{0.5})TiO_3$ ceramics. **Materials Chemistry and Physics**, 110, 311-315.

[50] Zhang, Y., Zheng, X. and Zhang, T. (2011). Characterization and humidity sensing properties of $Bi_{0.5}Na_{0.5}TiO_3$–$Bi_{0.5}K_{0.5}TiO_3$ powder synthesized by metal-organic decomposition. **Sensors and Actuators B: Chemical**, 156, 887-892.

[51] Liao, Y., Xiao, D., Lin, D., Zhu, J., Yu, P., Wu, L., et al. (2007). Synthesis and properties of $Bi0.5(Na_{1-x-y}K_xAg_y)_{0.5}TiO_3$ lead-free piezoelectric ceramics. **Ceramics International**, 33, 1445-1448.

[52] Yang, Z., Liu, B., Wei, L. and Hou, Y. (2008). Structure and electrical properties of $(1-x)Bi_{0.5}Na_{0.5}TiO_3$–$xBi_{0.5}K_{0.5}TiO_3$ ceramics near morphotropic phase boundary. **Materials Research Bulletin**, 43, 81-89.

[53] Zhou, C., Liu, X., Li, W. and Yuan, C. (2009). Structure and piezoelectric properties of $Bi_{0.5}Na_{0.5}TiO_3$–$Bi_{0.5}K_{0.5}TiO_3$–$BiFeO_3$ lead-free piezoelectric ceramics. **Materials Chemistry and Physics,** 114, 832-836.

[54] Zou, M., Fan, H., Chen, L. and Yang, W. (2010). Microstructure and electrical properties of (1-x)[$0.82Bi_{0.5}Na_{0.5}TiO_3$–$0.18Bi_{0.5}K_{0.5}TiO_3$]–x$BiFeO_3$ lead-free piezoelectric ceramics. **Journal of Alloys and Compounds**, 495, 280-283.

[55] Kantha, P., Pengpat, K., Jarupoom, P., Intatha, U., Rujijanagul, G. and Tunkasiri, T. (2009). Phase formation and electrical properties of BNLT–BZT lead-free piezoelectric ceramic system. **Current Applied Physics,** 9, 460-466.

[56] Moura, F., Simões, A. Z., Stojanovic, B. D., Zaghete, M. A., Longo, E. and Varela, J. A. (2008). Dielectric and ferroelectric characteristics of barium zirconate titanate ceramics prepared from mixed oxide method. **Journal of Alloys and Compounds**, 462, 129-134.

[57] Sumang, R., Vittayakorn, N. and Bongkarn, T. (2013). Crystal structure, microstructure and electrical properties of $(1-x-y)Bi_{0.5}Na_{0.5}TiO_3$–$xBi_{0.5}K_{0.5}TiO_3$–$yBiFeO_3$ ceramics near MPB prepared via the combustion technique. **Ceramics International**, 39 (1), S409-S413.

[58] Razak, K. A., Yip, C. J. and Sreekantan, S. (2011). Synthesis of $(Bi_{0.5}Na_{0.5})TiO_3$ (BNT) and Pr doped BNT using the soft combustion technique and its properties. **Journal of Alloys and Compounds**, 509, 2936-2941

[59] Julphunthong, P., Chootin, S. and Bongkarn, T. (2013). Phase formation and electrical properties of $Ba(Zr_xTi_{1-x})O_3$ ceramics synthesized through a novel combustion technique. **Ceramics International**, 39, S415-S419.

[60] Lin, D., Kwok, K. W. and Chan, H. L. W. (2008). Structure and electrical properties of $Bi_{0.5}Na_{0.5}TiO_3$–$BaTiO_3$–$Bi_{0.5}Li_{0.5}TiO_3$ lead-free piezoelectric ceramics. **Solid State Ionics**, 178, 1930-1937.

[61] Tian, Y., Wei, L., Chao, X., Liu, Z. and Yang, Z.(2013). Phase transition behavior and large piezoelectricity near the morphotropic phase boundary of lead-Free $(Ba_{0.85}Ca_{0.15})(Zr_{0.1}Ti_{0.9})O_3$ Ceramics. **J. Am. Ceram. Soc.**, 96, 496–502.

[62] Shieh, J., Wu, K. C. and Chen, C. S. (2007). Switching characteristics of MPB compositions of $(Bi_{0.5}Na_{0.5})TiO_3$–$BaTiO_3$–$(Bi_{0.5}K_{0.5})TiO_3$ lead-free ferroelectric ceramics. **Acta Materialia**, 55, 3081-3087.